Statistical properties of thermal Sunyaev–Zel'dovich maps

Dipak Munshi,[1]★ Shahab Joudaki,[2] Joseph Smidt,[2] Peter Coles[1] and Scott T. Kay[3]

[1]*School of Physics and Astronomy, Cardiff University, Queen's Buildings, 5 The Parade, Cardiff, CF24 3AA*
[2]*Department of Physics and Astronomy, University of California, Irvine, CA 92697, USA*
[3]*Jodrell Bank Centre for Astrophysics, The University of Manchester, Alan Turing Building, Manchester, M13 9PL*

ABSTRACT

On small angular scales, i.e. at high angular frequencies, beyond the damping tail of the primary power spectrum, the dominant contribution to the power spectrum of cosmic microwave background temperature fluctuations is the thermal Sunyaev–Zel'dovich (tSZ) effect. We investigate various important statistical properties of the Sunyaev–Zel'dovich maps, using well-motivated models for dark matter clustering to construct statistical descriptions of the tSZ effect to all orders enabling us to determine the entire probability distribution function (PDF). Any generic deterministic biasing scheme can be incorporated in our analysis and the effects of projection, biasing and the underlying density distribution can be analysed separately and transparently in this approach. We introduce the *cumulant correlators* as tools to analyse tSZ catalogues and relate them to corresponding statistical descriptors of the underlying density distribution. The statistics of hot spots in frequency-cleaned tSZ maps are also developed in a self-consistent way to an arbitrary order, to obtain results complementary to those found using the halo model. We also consider different beam sizes to check the extent to which the PDF can be extracted from various observational configurations. The formalism is presented with two specific models for underlying matter clustering, the hierarchical ansatz and the lognormal distribution. We find both models to be in very good agreement with the simulation results, though the extension of the hierarchical model has an edge over the lognormal model. In addition to testing against simulations made using semi-analytical techniques, we have also used the maps made using Millennium Gas Simulations to prove that the PDF and bias can indeed be predicted with very high accuracy using these models. The presence of significant non-gravitational effects such as preheating, however, cannot be modelled using an analytical approach which is based on the modelling of gravitational clustering alone. Our results indicate that the PDFs we construct are insensitive to the underlying cosmology and can thus provide a useful probe of non-gravitational processes, e.g. preheating or feedback.

Key words: cosmology: cosmic background radiation – cosmology: theory – cosmology: diffuse radiation – cosmology: large-scale structure of Universe.

1 INTRODUCTION

The inverse Compton scattering of cosmic microwave background (CMB) photons – known as the thermal Sunyaev–Zel'dovich (tSZ) effect (Sunyaev & Zel'dovich 1972, 1980; Rephaeli 1995; Birkinshaw 1999) – imprints a characteristic distortion in the CMB spectrum that can be studied using surveys such as *Wilkinson Microwave Anisotropy Probe* (*WMAP*)[1] and the ongoing *Planck*[2] satellite mission. The fluctuation of this distortion across the sky as probed by CMB observations can thus provide valuable clues to the fluctuations of the gas density and temperature. The up-scattering in frequency of CMB photons implies an increment in the spectrum at high frequencies with a corresponding decrement in the low-frequency (Rayleigh–Jeans, RJ) regime, and a null around 217 GHz. This characteristic behaviour is a potential tool for the separation of tSZ from the other temperature anisotropy contributions. These techniques are extremely effective in subtraction of primary

---

★ E-mail: Dipak.Munshi@astro.cf.ac.uk
[1] http://wmap.gsfc.nasa.gov/
[2] http://www.rssd.esa.int/Planck

anisotropies due to their well-understood (perfect blackbody) frequency dependence and near-Gaussian statistical behaviour (Bouchet & Gispert 1999; Delabroullie, Cardoso & Patanchon 2003; Leach et al. 2008). The tSZ effect is now routinely imaged in massive galaxy clusters where the temperature of the scattering medium can reach as high as 10 keV. This in effect produces a change in CMB temperature of the order of 1 mK at RJ wavelengths.

Here we are interested in the general intergalactic medium (IGM) where the gas is expected to be at ≤ 1 keV in the sort of mild overdensities that lead to CMB contributions in the μK range. In this work we primarily focus on the statistical study of wide-field CMB data where tSZ effects lead to anisotropies in the temperature distribution both due to resolved and unresolved galaxy clusters, keeping in mind that the tSZ contribution is the dominant signal beyond the damping tail of the primary anisotropy power spectrum. We primarily focus on analytical modelling of the entire one and the joint two-point probability distribution function (PDF) of the tSZ effect.

The tSZ power spectrum is known to be a sensitive probe of the amplitude of density fluctuations. Higher order statistics such as the skewness or bispectrum can provide independent estimates on the bias associated with baryonic pressure, as well as providing further consistency checks and cross-validation of lower order estimates. The modelling of lower order statistics of the tSZ effect done by various authors (Cooray 2000; Seljak 2000; Cooray 2001b; Zhang & Pen 2001; Komatsu & Seljak 2002; Zhang & Seth 2007) in the past has followed the halo model (Cooray & Seth 2002) that relies on ingredients for the mass function based on the Press–Schechter (PS; Press & Schechter 1974) formalism and radial profile given by Navarro, Frenk & White (1996).

In addition to analytical modelling, the numerical simulation of tSZ plays an important role in our understanding of the physics involved (Persi et al. 1995; da Silva et al. 2000; Refregier et al. 2000; Seljak, Burwell & Pen 2000; Springel, White & Hernquist 2001; Refregier & Teyssier 2002; White, Hernquist & Springel 2002; Lin et al. 2004; Zhang, Pen & Trac 2004; Cao, Liu & Fang 2007; Hallman et al. 2007, 2009; Roncarelli et al. 2007; Scott et al. 2012).Though limited by their dynamic range, some of these studies incorporate complication from additional radiative and hydrodynamical effects (i.e. 'gastrophysics') such as radiative cooling, preheating and supernova (SN)/active galactic nucleus (AGN) feedback to a certain extent which are otherwise difficult to incorporate in any analytical calculations.

In parallel with the development of this PS formalism, analytical modelling based on hierarchical form for the higher order correlation functions has also been studied extensively (Szapudi, Szalay & Boschan 1992; Szapudi & Szalay 1993; Szapudi & Colombi 1996; Szapudi & Szalay 1997; Bernardeau et al. 2002). We employ the particular form proposed by Balian & Schaeffer (1989) to model the tSZ statistics. This form has been studied extensively in the literature for modelling weak lensing as well for the statistics of collapsed objects and a related astrophysical phenomenon. The statistics of collapsed objects and their contribution to the tSZ sky have been studied previously (Valageas & Silk 1999; Valageas, Schaeffer & Silk 2002). These studies also probe X-ray luminosity from the same clusters. In this study we do not probe individual clusters or collapsed objects, but instead directly link the density field with corresponding SZ observables. Though the diffuse component of the tSZ effect is beyond *WMAP* detection threshold, the situation may improve with future data sets such as Planck (Hansen et al. 2005; Joudaki et al. 2010) or surveys such as Arcminute Cosmology Bolometer Array Receiver (ACBAR; see Runyan et al. 2003)[3]

The paper is organized as follows. In Section 2 we provide the details of the tSZ effect. We link the higher order multispectra of the SZ effect with the underlying mass distribution with the help of various biasing schemes in Section 3. In Section 4 we introduce the generic hierarchical *ansatz* and in Section 5 we introduce the specific formalism based on generating functions in the quasi-linear and highly non-linear regimes. In Section 6 we show how the PDF and bias of the tSZ sky are related to the underlying density PDF and bias. Various approximation schemes are discussed that can be used to simplify the PDF and bias. In Section 7 we describe various simulations we have used in our study. In Section 8 we present the results of tests against simulations. Finally, the Section 9 is dedicated to the discussion of our result and future prospects.

2 FORMALISM

In this section we will provide necessary theoretical background for the computation of lower order moments of tSZ both for the one-point cumulants and the two-point cumulant correlators. These will be later used to construct the entire PDF and the bias of tSZ in the context of hierarchical clustering. We will be using the following form of the Robertson–Walker line element for the background geometry of the universe:

$$ds^2 = -c^2 dt^2 + a^2(t)\left[dr^2 + d_A^2(r)(d\theta^2 + \sin^2\theta d\phi^2)\right]. \tag{1}$$

Here we have denoted the comoving angular diameter distance by $d_A(r)$ and scale factor of the universe by $a(t)$. $d_A(r) = K^{-1/2}\sin(K^{+1/2}r)$ for positive curvature, $d_A(r) = (-K)^{-1/2}\sinh((-K)^{+1/2}r)$ for negative curvature and r for a flat universe. Here r is comoving distance or lookback time. For a present value of H_0 and Ω_0 we have $K = (\Omega_0 + \Omega_\Lambda - 1)H_0^2$. The tSZ temperature fluctuation $\Delta T_{SZ}(\hat{\Omega}, \nu) = \delta T(\hat{\Omega}, \nu)/T_{CMB}$ is given by the opacity-weighted electron pressure:

$$\Delta T_{SZ}(\hat{\Omega}, \nu) \equiv g_\nu(x_\nu)y(\hat{\Omega}) = g_\nu(x_\nu)\int_0^{r_0} dr\, \dot{\tau}_e\, \pi_e(\hat{\Omega}, r); \quad \pi_e(\boldsymbol{x}) = \delta p_e(\boldsymbol{x})/\langle p_e\rangle. \tag{2}$$

Here τ_e is the Thomson optical depth; overdots represent derivatives with respect to r. Here $y(\hat{\Omega})$ is the map of the Compton y parameter. The Thomson optical depth τ_e can be expressed in terms the Thompson cross-section σ_T and the Boltzman constant k_B by the integral

---

[3] http://cosmology.berkeley.edu/group/swlh/acbar/

$\tau_e = c \int n_e(z)\sigma_{\mathrm{T}}\,\mathrm{d}t$. The free electron number density is represented by $n_e(z)$. The function $g_\nu(x)$ encodes the frequency dependence of the tSZ anisotropies. It relates the temperature fluctuations at a frequency ν with the Compton parameter y. Here the function $g_\nu(x)$ is defined as $g_\nu(x_\nu) = x_\nu \coth(x_\nu/2) - 4$ with $x_\nu = h\nu/(k_{\mathrm{B}}T_{\mathrm{CMB}}) = \nu/(56.84\,\mathrm{GHz})$. In the low-frequency part of the spectrum $g_\nu(x_\nu) = -2$, for $x_\nu \ll 1$, here x_ν is the dimensionless frequency as defined above. We will primarily be working in the Fourier domain and will be using the following convention:

$$\pi_e(\boldsymbol{k};r) = \int \mathrm{d}^3\boldsymbol{x}\,\pi_e(\boldsymbol{x};r)\exp[-\mathrm{i}\boldsymbol{k}\cdot\boldsymbol{x}]. \tag{3}$$

The projected statistics that we will consider can be related to 3D statistics defined by the following expressions which specify the power spectrum $P_\pi(k;r)$, the bispectrum $B_\pi(k_1, k_2, k_3; r)$ and the trispectrum $T_\pi(k_1, k_2, k_3, k_4; r)$ in terms of the Fourier coefficients. In our notation we will separate the temporal dependence with a semicolon:

$$\langle\pi_e(\boldsymbol{k}_1;r)\pi_e(\boldsymbol{k}_2;r)\rangle_c = (2\pi)^3\delta_D(\boldsymbol{k}_1+\boldsymbol{k}_2)P_\pi(k_1;r);\ \ \langle\pi_e(\boldsymbol{k}_1;r)\pi_e(\boldsymbol{k}_2;r)\pi_e(\boldsymbol{k}_3;r)\rangle_c = (2\pi)^3 B_\pi(k_1, k_2, k_3;r)\delta_D(\boldsymbol{k}_1+\boldsymbol{k}_2+\boldsymbol{k}_3) \tag{4}$$

$$\langle\pi_e(\boldsymbol{k}_1;r)\pi_e(\boldsymbol{k}_2;r)\pi_e(\boldsymbol{k}_3;r)\pi_e(\boldsymbol{k}_4;r)\rangle_c = (2\pi)^3 T_\pi(k_1, k_2, k_3, k_4;r)\delta_D(\boldsymbol{k}_1+\boldsymbol{k}_2+\boldsymbol{k}_3+\boldsymbol{k}_4). \tag{5}$$

The subscript c denotes the *connected* parts of a cumulant, i.e. those parts not related to the lower order correlations. The multispectra of the underlying density field will develop a similar hierarchy. In the linear bias formalism, the multispectra of the field π are directly linked to the density contrast $\delta = (\rho_m - \langle\rho_m\rangle)/\langle\rho_m\rangle$ with ρ_m being the homogeneous background density of the Universe. Using a bias factor $b_\pi(r)$, which depends on redshift, we can write (Goldberg & Spergel 1999a,b; Cooray 2000, 2001b)

$$P_\pi(k_1;r) = b_\pi^2(r)P_\delta(k_1;r); \qquad B_\pi(k_1, k_2, k_3;r_i) = b_\pi^3(r)B_\delta(k_1, k_2, k_3;r_i); \qquad T_\pi(k_1, k_2, k_3, k_4;r_i) = b_\pi^4(r)T_\delta(k_1, k_2, k_3, k_4;r_i). \tag{6}$$

The redshift z_s dependence of the bias is typically assumed to be of the following form: $b_\pi(z_s) = b_\pi(0)/(1+z_s)$ and $b_\pi(0) = k_{\mathrm{B}}T_e(0)b_\delta/(m_ec^2)$. In our analysis we will show that it is possible to define a reduced y parameter whose statistics will be insensitive to the details of the biasing model. The biasing scheme is motivated by a tight correlation between baryonic pressure and the density contrast in high-density regions where most of the tSZ signals originate.

We have studied the correlation between the fractional baryonic gas pressure $P_{\mathrm{gas}}/\langle P_{\mathrm{gas}}\rangle$ and the density contrast $\rho_m/\langle\rho_m\rangle = 1 + \delta$ in Fig. 1. The electronic pressure p_e and the baryonic (gas) pressure P_{gas} are related (Cooray 2000, 2001a,b) by $p_e = \frac{3X+2}{3X+5}P_{\mathrm{gas}}$; here, $X = 0.76$ is the primordial hydrogen abundance. The 3D electronic pressure fluctuation π_e can be expressed as $1 + \pi_e = p_e/\langle p_e\rangle = P_{\mathrm{gas}}/\langle P_{\mathrm{gas}}\rangle$. We find a correlation between these two variables, i.e. δ and π_e. The correlation is tighter for regions with higher density contrast δ, where most of the tSZ signals originate. We have considered two smoothing scales. The top and bottom panels correspond to smoothing scales of 0.5 and $5\,h^{-1}$ Mpc, respectively. We have displayed $50\,000$ randomly selected points from the simulations used for our study at a redshift of $z = 0$. The left-hand panels correspond to the gravity-only (GO) simulations, whereas the right-hand panels correspond to simulations with preheating and are denoted by PC. The correlation is more pronounced for the GO simulations.
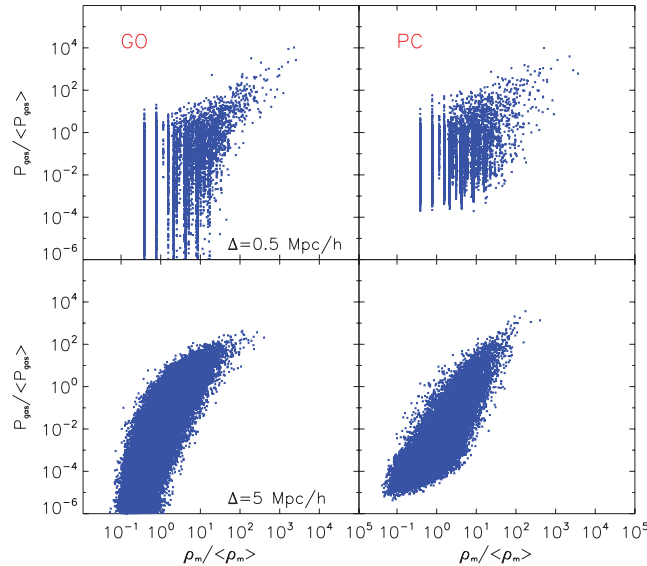

Figure 1. Scatter plots of the baryonic pressure versus the dark matter density contrast $1 + \delta = \rho_m/\langle\rho_m\rangle$ are displayed for various simulations used in our study at a redshift of $z = 0$. The left-hand panels correspond to the simulations with no preheating (i.e. gravity-only simulations but with adiabatic cooling), shown here as GO, whereas the right-hand panels correspond to the simulations with preheating, depicted as PC. More details about the simulations are presented in Section 7. The smoothing scale for these plots is $0.5\,h^{-1}$Mpc for the upper panels and $5\,h^{-1}$Mpc for the lower panels. The scatter is lower for regions with high density contrast $1 + \delta > 100$ where most of the tSZ signals originate. The simulations with preheating exhibit a less well-defined correlation structure. We have shown $50\,000$ randomly sampled points from our simulations in each panel.

Table 1. The notations for various statistics of $\delta(r)$, $\tilde{y}_s(\hat{\Omega})$ and $\hat{y}_s(\hat{\Omega})$ are tabulated. The parameter $\hat{y}$ is constructed to have the same statistics as δ under certain simplifying approximations, i.e. $\hat{h}(x) = h(x)$ and $\hat{b}(x) = b(x)$. The variance of $\delta(r)$ is however different compared to that of $\hat{y}_s(\hat{\Omega})$. Also, note that $\delta(r)$ is a 3D field whereas $\hat{y}(\hat{\Omega})$ is a projected (or 2D) field. The normalized cumulants of $\hat{y}(\hat{\Omega})$ and $\delta(r)$ are identical, under certain approximations. Hence, they are independent of the biasing. The variance of these fields is however different.

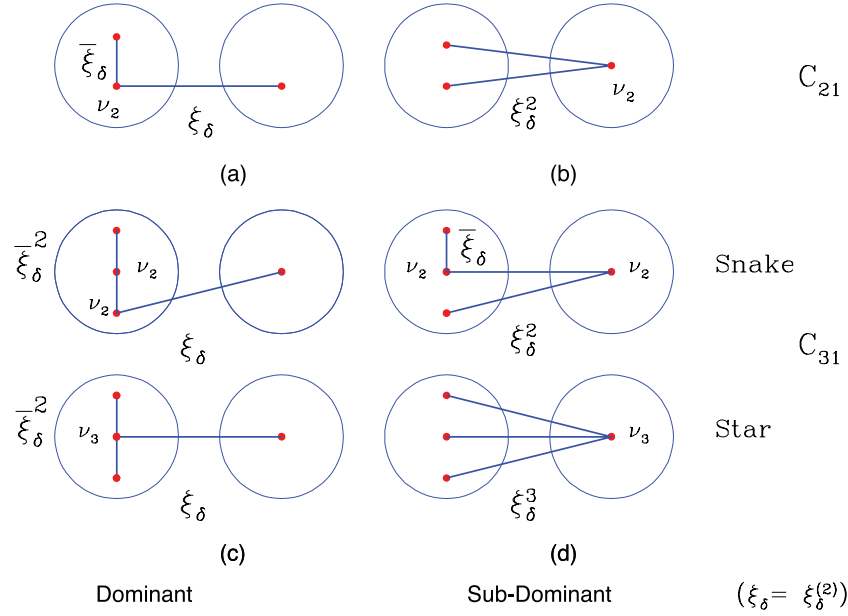|	Cumu.	Cor.	VPF	2VPF	1PDF	2PDF
$\delta(r)$	S_p	C_{pq}	$\phi(z)$	$\beta(z)$	$h(x)$	$b(x)$
$\tilde{y}_s(\hat{\Omega})$	$\tilde{S}_p$	$\tilde{C}_{pq}$	$\tilde{\Phi}(z)$	$\tilde{\beta}(z)$	$\tilde{h}(x)$	$\tilde{b}(x)$
$\hat{y}_s(\hat{\Omega})$	$\hat{S}_p$	$\hat{C}_{pq}$	$\hat{\Phi}(z)$	$\hat{\beta}(z)$	$\hat{h}(x)$	$\hat{b}(x)$

Dominant and Sub−dominant Contributions

Figure 2. A selection of diagrams that contribute to the cumulant correlators C_{21} and C_{31} are depicted. At the lowest order in non-Gaussianity, the cumulant correlator C_{21} has two distinct contributions. The dominant contribution comes from diagram (a). The other contribution from diagram (b) adds negligible contribution because of the multiplicative factor $(\bar{\xi}_\delta^{(2)}/\bar{\xi}_\delta^{(2)})$. Here $\xi_\delta^{(2)}$ is the correlation function and $\bar{\xi}_\delta^{(2)}$ is its average over the 'cell' volume. We have suppressed the superscripts for brevity. The two diagrams denoted by (c) show a representative dominant contribution to C_{31}. The diagrams denoted by (d) show the subdominant contributions to C_{31}. The upper panels of diagrams (c) and (d) are of *snake* topology, whereas the bottom panels correspond to the *star* topology. In our analysis we have ignored the subdominant term which is negligible when the cells are separated far apart.

3 LOWER ORDER STATISTICS OF THE TSZ EFFECT

The statistics of the smoothed tSZ effect $\hat{y}_s = (y_s - \langle y_s \rangle)/\langle y \rangle$ reflect those of the baryonic pressure fluctuations projected along the line of sight. Note that in the denominator we have the average of unsmoothed y parameter. In our analysis we will consider a small patch of the sky where we can use the plane-parallel (or small-angle) approximation to replace spherical harmonics by Fourier modes. The three-dimensional electronic pressure fluctuations $\pi_e(\mathbf{x})$ along the line of sight when projected on to the sky with the weight function $\omega_{SZ}(r)$ give the tSZ effect in a direction $\hat{\Omega}$ which we denote by $y(\hat{\Omega})$ [the smoothed y maps will be denoted by $y_s(\hat{\Omega})$ where the subscript s will denote smoothed quantities – see Table 1 for notations:

$$y_s(\hat{\Omega}) = \int_0^{r_s} dr\, \omega_{SZ}(r)\, \pi_e(r, \hat{\Omega}); \quad \omega_{SZ}(r) = \dot{t}_e(r); \quad y_s(\hat{\Omega}) = \int d\hat{\Omega}' W_G(\hat{\Omega} - \hat{\Omega}'; \theta_b) y(\hat{\Omega}'). \tag{7}$$

Throughout, we will be using a Gaussian window W_G, or equivalently a Gaussian beam b_l in the harmonic domain, specified by its full width at half-maxima or FWHM $= \theta_b$. Using the small-angle approximation we can compute the projected two-point correlation function in terms of the dark matter power spectrum $P_\delta(k, r)$ (Kaiser 1992):

$$\langle \tilde{y}_s(\hat{\Omega}_1)\tilde{y}_s(\hat{\Omega}_2) \rangle_c = \int_0^{r_s} dr\, \frac{\omega_{SZ}^2(r)}{d_A^2(r)} \int \frac{d^2 l}{(2\pi)^2}\, \exp(i\,\boldsymbol{\theta}_{12} \cdot \boldsymbol{l})\, b_l^2(\theta_b) P_\pi\left[\frac{l}{d_A(r)}; r\right]; \quad \tilde{y}_s = y_s - \langle y_s \rangle. \tag{8}$$

Here θ_{12} is the angular separation projected on to the surface of the sky and we have also introduced $\boldsymbol{l} = d_A(r)\boldsymbol{k}_\perp$ to denote the scaled projected wave vector. Using Limber's approximation (Limber 1954), the variance and higher order moments of y_s, smoothed using a Gaussian beam: $b_l(\theta_b) = \exp[-l(l+1)\sigma_b]$; $\sigma_b = \frac{\theta_b}{\sqrt{8\ln(2)}}$ with $\text{FWHM} = \theta_b$, can be written as

$$\langle \tilde{y}_s^p(\theta_b)\rangle_c = \int_0^{r_s} dr \frac{\omega_{SZ}^p(r)}{d_A^{2(p-1)}(r)} \int \frac{d^2\boldsymbol{l}_1}{(2\pi)^2} b_{l_1}(\theta_b) \cdots \int \frac{d^2\boldsymbol{l}_{p-1}}{(2\pi)^2} b_{l_{p-1}}(\theta_b)\, b_{l_p}(\theta_b)\, B_\pi^{(p)}\left(\frac{\boldsymbol{l}_1}{d_A(r)},\cdots,\frac{\boldsymbol{l}_p}{d_A(r)}, r\right)\delta_D(\boldsymbol{l}_1 + \cdots + \boldsymbol{l}_p). \tag{9}$$

The higher order moments of the smoothed temperature field relate $\langle \tilde{y}_s^p(\theta_b)\rangle_c$ to the three-dimensional multispectra of the underlying pressure fluctuations $B_\pi^{(p)}$ (Hui 1999; Munshi & Coles 2000). We will use these results to show that it is possible to compute the complete PDF of y_s from the underlying dark matter PDF. Details of the analytical results presented here can be found in Munshi, Coles & Melott (1999a,b), Munshi, Melott & Coles (2000) and Munshi & Coles (2000). A similar analysis for the higher order cumulant correlators (Szapudi & Szalay 1997; Munshi et al. 2000) of the smoothed SZ field relating $\langle \tilde{y}_s^p(\hat{\Omega}_1)\tilde{y}_s^q(\hat{\Omega}_2)\rangle_c$ to multispectra of pressure fluctuation $B_\pi^{(p+q)}$ can be expressed as (Munshi & Coles 2000)

$$\langle \tilde{y}_s^p(\hat{\Omega}_1)\tilde{y}_s^q(\hat{\Omega}_2)\rangle_c = \int_0^{r_s} \frac{\omega_{SZ}^{p+q}(r)}{d_A^{2(p+q-1)}(r)} dr \int \frac{d^2\boldsymbol{l}_1}{(2\pi)^2} b_{l_1}(\theta_b) \cdots \int \frac{d^2\boldsymbol{l}_{p+q-1}}{(2\pi)^2} b_{l_{p+q-1}}(\theta_b) b_{l_{p+q}}(\theta_b)\exp(i\,(\boldsymbol{l}_1 + \cdots + \boldsymbol{l}_p)\cdot\theta_{12})$$
$$\times\, B_\pi^{(p+q)}\left(\frac{\boldsymbol{l}_1}{d_A(r)},\ldots,\frac{\boldsymbol{l}_{p+q}}{d_A(r)}, r\right)\delta_D(\boldsymbol{l}_1 + \cdots + \boldsymbol{l}_{p+q}). \tag{10}$$

We will use and extend these results in this paper to show that it is possible to compute the entire bias function $b(> \hat{y}_s)$, i.e. the bias associated with those spots in the tSZ map where $\hat{y}_s$ is above certain threshold, from the statistics of underlying overdense dark objects; this then acts as a generating function for the cumulant correlators. Details of the analytical results presented here can be found in Munshi & Coles (2000).

4 HIERARCHICAL *ANSATZ*: THE MINIMAL TREE MODEL AND ITS EXTENSION

The spatial length scales corresponding to the small angular scales of relevance here are in the highly non-linear regime. Assuming a *tree model* for the matter correlation hierarchy in the highly non-linear regime for the density contrast δ, one can write the general form of the Nth order correlation function $\xi_\delta^{(N)}$ in terms of the two-point correlation function $\xi_\delta^{(2)}$ (Peebles 1980; Fry 1984; Bernardeau 1992, 1994):

$$\xi_\delta^{(N)}(\boldsymbol{r}_1,\ldots,\boldsymbol{r}_N) = \sum_{\alpha,N-\text{trees}} Q_{N,\alpha} \sum_{\text{labellings}} \prod_{\text{edges}}^{(N-1)} \xi_\delta^{(2)}(\boldsymbol{r}_i,\boldsymbol{r}_j). \tag{11}$$

It is interesting to note that a similar hierarchy develops in the quasi-linear regime in the limit of vanishing variance (Bernardeau & Schaeffer 1992). However, the hierarchical amplitudes $Q_{N,\alpha}$ become shape-dependent functions in the quasi-linear regime. In the highly non-linear regime there are some indications that these functions become independent of shape, as suggested by studies of the lowest order parameter $Q_3 = Q$ using high-resolution numerical simulations (Scoccimarro & Frieman 1999). In Fourier space such an *ansatz* means that the hierarchy of multispectra can be written as sums of products of the matter power spectrum:

$$B_\delta(\boldsymbol{k}_1,\boldsymbol{k}_2,\boldsymbol{k}_3) = Q(P_\delta(k_1)P_\delta(k_2) + P_\delta(k_2)P_\delta(k_3) + P_\delta(k_3)P_\delta(k_1));$$
$$T_\delta(\boldsymbol{k}_1,\boldsymbol{k}_2,\boldsymbol{k}_3,\boldsymbol{k}_4) = R_a\, P_\delta(k_1)P_\delta(|\boldsymbol{k}_1 + \boldsymbol{k}_2|)P_\delta(|\boldsymbol{k}_1 + \boldsymbol{k}_2 + \boldsymbol{k}_3|) + \text{cyc.perm.} + R_b\, P_\delta(k_1)P_\delta(k_2)P_\delta(k_3) + \text{cyc. perm.} \tag{12}$$

Different hierarchical models differ in the way they predict the amplitudes of different tree topologies (Munshi et al. 1999a,b, 2000).

Working directly with cumulant generating function $\phi(y)$ (to be introduced later), modelling of the entire PDF was achieved by Colombi et al. (1997). Remarkably, this was possible by a simple empirical modification of the existing quasi-linear predictions and was dubbed extended perturbation theory (EPT). The characteristic feature of this approach was to treat the local slope of the linear power spectrum as a free parameter in order to extend perturbative results to the non-linear regime. EPT is fully parametrized by the non-linear variance and the skewness or equivalently Q_3 which is predicted by hyperextended perturbation theory (HEPT) developed by Scoccimarro & Frieman (1999).

In recent years a new semi-analytical model for PDF has been proposed by Valageas & Munshi (2004).[4] Its construction is very similar to EPT and works directly with $\phi(y)$. In addition to imposing the quasi-linear regime it also satisfies the rare void limit. We will use this approach and show that the formalism is reasonably accurate in predicting the tSZ PDF.

4.1 Cumulants

Using this model we can express the one-point cumulants $\tilde{S}_N$ of $\tilde{y}_s = y_s - \langle y_s\rangle$ as

$$\langle \tilde{y}_s^3(\theta_b)\rangle_c = (3Q_3)\mathcal{C}_3[\mathcal{I}_{\theta_b}^2] \equiv S_3\mathcal{C}_3[\mathcal{I}_{\theta_b}^2] = \tilde{S}_3\langle \tilde{y}_s^2(\theta_b)\rangle_c^2; \tag{13}$$

$$\langle \tilde{y}_s^4(\theta_b)\rangle_c = (12R_a + 4R_b)\mathcal{C}_4[\mathcal{I}_{\theta_b}^3] \equiv S_4\mathcal{C}_4[\mathcal{I}_{\theta_b}^3] = \tilde{S}_4\langle \tilde{y}_s^2(\theta_b)\rangle_c^3. \tag{14}$$

---

[4] http://ipht.cea.fr/Pisp/patrick.valageas/codepdf_en.php

In general, for an arbitrary order cumulant we can write

$$\langle \tilde{y}_s^p(\theta_b) \rangle_c = S_p \mathcal{C}_p[[\mathcal{I}_{\theta_b}]^{p-1}]; \quad \mathcal{C}_p\left[[\mathcal{I}_{\theta_b}]^{p-1}\right] = \int_0^{r_s} \frac{\omega_{\mathrm{SZ}}^p(r) b_\pi^p(r)}{d_{\mathrm{A}}^{2(p-1)}(r)} [\mathcal{I}_{\theta_b}]^{(p-1)} dr; \qquad [\mathcal{I}_{\theta_b}] = \int \frac{d^2 l}{(2\pi)^2} P_\delta\left(\frac{l}{d_{\mathrm{A}}(r)}\right) b_l^2(\theta_b). \tag{15}$$

The projection effects on density cumulants were first derived in Bernardeau, van Waerbeke & Mellier (1997). In the context of weak-lensing surveys, equation (13) was derived by Hui (1999). Note that equation (15) relates the normalized one-point cumulants of $\tilde{y}_s$, i.e. $\tilde{S}_p$, to those of the underlying density contrast S_p.

We will define a parameter $\hat{y}_s = \tilde{y}_s / \langle y \rangle$ which will further simplify the results. In particular we will find that, under certain simplifying assumptions, the statistics of $\tilde{y}$ are identical to those of the underlying density contrast δ. Note that the definition of the parameter $\hat{y}_s$ involves the unsmoothed $\langle y_s \rangle$ in the denominator. The normalized cumulants of $\hat{y}_s$ will be denoted as $\hat{S} = \langle \hat{y}_s^p \rangle_c / \langle \hat{y}_s^2 \rangle_c^{(p-1)}$, which can be expressed as $\hat{S} = \tilde{S} \langle y \rangle^{(p-1)}$.

4.2 Cumulant correlators

The concept of cumulant correlators was introduced by Bernardeau (1996). Later studies extended this result to observational studies including weak-lensing statistics (Munshi & Coles 2000; Munshi & Jain 2000, 2001). In the present context, the family of cumulant correlators is important in modelling the bias associated with y maps,

$$\langle \tilde{y}_s^2(\hat{\Omega}_1) \tilde{y}_s(\hat{\Omega}_2) \rangle_c = 2 Q_3 \mathcal{C}_3 [\mathcal{I}_{\theta_b} \mathcal{I}_{\theta_{12}}] \equiv C_{21} \mathcal{C}_3 [\mathcal{I}_{\theta_b} \mathcal{I}_{\theta_{12}}] \equiv \tilde{C}_{21} \langle \tilde{y}_s^2 \rangle_c \langle \tilde{y}_s(\hat{\Omega}_1) \tilde{y}_s(\hat{\Omega}_2) \rangle_c, \tag{16}$$

$$\langle \tilde{y}_s^3(\hat{\Omega}_1) \tilde{y}_s(\hat{\Omega}_2) \rangle_c = (3R_a + 6R_b) \mathcal{C}_4 [\mathcal{I}_{\theta_b}^2 \mathcal{I}_{\theta_{12}}] \equiv \tilde{C}_{31} \langle \tilde{y}_s^2 \rangle_c^2 \langle \tilde{y}_s(\hat{\Omega}_1) \tilde{y}_s(\hat{\Omega}_2) \rangle_c. \tag{17}$$

In general, for an arbitrary order cumulant correlator we can write

$$\langle \tilde{y}_s^p(\hat{\Omega}_1) \tilde{y}_s^q(\hat{\Omega}_2) \rangle_c \equiv C_{pq} \mathcal{C}_{p+q} [[\mathcal{I}_{\theta_b}]^{p+q-2} \mathcal{I}_{\theta_{12}}] = \tilde{C}_{pq} \langle \tilde{y}_s^2 \rangle_c^{(p+q-2)} \langle \tilde{y}_s(\hat{\Omega}_1) \tilde{y}_s(\hat{\Omega}_2) \rangle_c, \tag{18}$$

where we have introduced the following notation:

$$\mathcal{C}_{p+q}[[\mathcal{I}_{\theta_b}]^{(p+q-2)} \mathcal{I}_{\theta_{12}}] = \int_0^{r_s} \frac{\omega_{\mathrm{SZ}}^{p+q}(r) b_\pi^{p+q}(r)}{d_{\mathrm{A}}^{2(p+q-1)}(r)} [\mathcal{I}_{\theta_b}]^{p+q-2} [\mathcal{I}_{\theta_{12}}] \, dr; \qquad [\mathcal{I}_{\theta_{12}}] = \int \frac{d^2 l}{(2\pi)^2} P_\delta\left(\frac{l}{d_{\mathrm{A}}(r)}\right) b_l^2(\theta_b) \exp(i l \cdot \theta_{12}). \tag{19}$$

Note that in the limiting case of $\theta_{12} = 0$ we recover the limiting situation $\tilde{C}_{pq} = \tilde{S}_{p+q}$ since we have $[\mathcal{I}_{\theta_b}] = \mathcal{I}_{\theta_{12}}$. The cumulant correlators for $\hat{y}$ denoted as $\hat{C}_{pq}$ and $\tilde{y}$ are related by the expression $\hat{C}_{pq} = \tilde{C}_{pq} \langle y \rangle^{p+q-1}$.

These lowest order statistics can be helpful in probing the pressure bias as a function of scale. It is however expected that the signal-to-noise ratio will decrease with increasing order. We will use these results to construct the entire PDF and the bias associated with the tSZ maps. This will be achieved using a generating function approach. In Fig. 2 we have shown some of the lower order C_{pq} using tree-level diagrams.

5 THE GENERATING FUNCTION

To go beyond order-by-order approach discussed so far we will use a formalism based on generating functions, which relies on the hierarchical scaling nature of the higher order correlation function. The scaling analysis deals directly with the generating functions that encode the information regarding the correlation hierarchy. The knowledge of these generating functions is next useful in constructing the one-point and two-point PDFs.

In scaling analysis of the PDF, the void probability distribution function (VPF) plays a most fundamental role, because it can be related to the generating function $\phi(z)$ of the cumulants or, if preferred, the S_p parameters (White 1979; Balian & Schaeffer 1989):

$$P_v(0) = \exp\left(-\frac{\phi(N_c)}{\bar{\xi}_\delta^{(2)}}\right), \tag{20}$$

where $P_v(0)$ is the probability of having no 'particles' in a cell of volume v, $\bar{N}$ is the average occupancy of these 'particles', $N_c = \bar{N} \bar{\xi}_\delta^{(2)}$ and $\bar{\xi}_\delta^{(2)}$ is the volume average of the two-point correlation function $\xi_\delta^{(2)}$. Strictly speaking, the above expression neglects any residual (subleading) $\bar{\xi}_\delta^{(2)}$ dependence of the S_p parameters. The VPF is meaningful only for the discrete distribution of particles and cannot be defined for smooth density fields such as δ or $\hat{y}_s(\hat{\Omega})$. However, the scaling function $\phi(z)$ defined above is very much useful even for continuous distributions where they can be used as a generating function of one-point cumulants or S_p parameters: $\phi(z) = \sum_{p=1}^{\infty} S_p z^p / p!$. The function $\phi(z)$ satisfies the constraint $S_1 = S_2 = 1$ necessary for proper normalization of the PDF. The other generating function which plays a very important role in such analysis is the generating function for vertex amplitudes ν_n, associated with nodes appearing in a 'tree' representation of higher order correlation hierarchy ($Q_3 = \nu_2$, $R_a = \nu_2^2$ and $R_b = \nu_3$). In practice, it is possible to work with a perturbative expansion of the vertex generating function $\mathcal{G}(\tau)$. In terms of the vertices it is defined as $\mathcal{G}(\tau) = \sum_{n=0}^{\infty} (-\tau)^n \nu_n / n!$. However, in the highly non-linear regime a closed

form is used. A more specific model for $\mathcal{G}(\tau)$, which is useful to make more specific predictions (Bernardeau & Schaeffer 1992), is given by $\mathcal{G}(\tau) = (1 + \tau/\kappa_a)^{-\kappa_a}$;

$$\phi(z) = z\mathcal{G}(\tau) - \frac{1}{2}z\tau\frac{\mathrm{d}}{\mathrm{d}\tau}\mathcal{G}(\tau); \qquad \tau = -z\frac{\mathrm{d}}{\mathrm{d}\tau}\mathcal{G}(\tau). \tag{21}$$

The range of δ for which the power-law regime is valid depends on the value of $\bar{\xi}_\delta^{(2)}$. For smaller values of $\bar{\xi}_2$, the power-law regime is less pronounced. A more detailed discussion of these issues can be found in Munshi et al. (1999). The links to the gravitational dynamics in the quasi-linear regime for various approximations are discussed in Munshi, Sahni & Starobinsky (1994). The second equation of (21) defines the variable z in terms of τ, which can then be used to construct the function $\phi(z)$ for a given model of $\mathcal{G}(\tau)$. However, a more detailed analysis is needed to include the effect of correlation between two or more correlated volume elements which will provide information about bias, cumulants and cumulant correlators of these collapsed objects (as opposed to the cumulants and cumulant correlators of the whole map; e.g. Munshi & Jain 2000, 2001). We will only quote results useful for measurement of bias; detailed derivations of related results including related error analysis can be found elsewhere (Bernardeau & Schaeffer 1999; Coles, Melott & Munshi 1999; Munshi et al. 1999a,b, 2000).

Note that $\tau(z)$ [also denoted by $\beta(z)$ in the literature] plays the role of a generating function for factorized cumulant correlators C_{p1} ($C_{pq} = C_{p1}C_{q1}$): $\tau(z) = \sum_{p=1}^{\infty} C_{p1}/p!z^p$. The PDF $p(\delta)$ and bias $b(\delta)$ can be related to their generating functions VPF $\phi(z)$ and $\tau(z)$, respectively, by following equations (Balian & Schaeffer 1989; Bernardeau & Schaeffer 1992, 1999)[5]:

$$p(\delta) = \int_{-i\infty}^{i\infty}\frac{\mathrm{d}z}{2\pi i}\exp\left[\frac{(1+\delta)z - \phi(z)}{\bar{\xi}_\delta^{(2)}}\right]; \quad b(\delta)p(\delta) = \int_{-i\infty}^{i\infty}\frac{\mathrm{d}z}{2\pi i}\tau(z)\exp\left[\frac{(1+\delta)z - \phi(z)}{\bar{\xi}_\delta^{(2)}}\right]. \tag{22}$$

It is clear that the function $\phi(z)$ completely determines the behaviour of the PDF $p(\delta)$ for all values of δ. The PDF too can be expressed with the help of a scaling function:

$$p(\delta) = \frac{h(x)}{[\bar{\xi}_\delta^{(2)}]^2}; \qquad x = \frac{(1+\delta)}{\bar{\xi}_\delta^{(2)}}. \tag{23}$$

The scaling function $h(x)$ is related to $\phi(z)$ through an inverse Laplace transform:

$$h(x) = -\frac{1}{2\pi i}\int_{-i\infty}^{+i\infty}\mathrm{d}z\exp(xz)\phi(z); \qquad h(x)b(x) = -\frac{1}{2\pi i}\int_{-i\infty}^{+i\infty}\mathrm{d}z\exp(xz)\beta(z). \tag{24}$$

The quantities $\phi(z)$ and $\beta(z)$ correspond to the density contrast δ, and $\hat{\Phi}(z)$ and $\hat{\beta}(z)$ will denote corresponding quantities for $\hat{y}_s$. The functions $b(x)$ is simply a scaled version of $b(\delta)$:

$$b(x) = b\left(\frac{1+\delta}{\bar{\xi}_\delta^{(2)}}\right). \tag{25}$$

We will next use these expressions to analyse the PDF and bias of $y(\hat{\Omega})$ maps.

6 THE PDF AND THE BIAS OF THE BEAM-SMOOTHED SZ EFFECT

For computing the PDF of the smoothed scaled tSZ field, we will use the variable $\tilde{y}_s$ that will make the analysis simpler: $\tilde{y}_s(\theta_b) = y_s(\theta_b) - \langle y_s(\theta_b)\rangle$, we will begin by constructing its associated cumulant generating function $\tilde{\Phi}(z)$:

$$\tilde{\Phi}(z) = \sum_{p=1}^{\infty}\tilde{S}_p\frac{z^p}{p!} = \sum_{p=1}^{\infty}\frac{\langle\tilde{y}_s^p(\theta_b)\rangle_c}{\langle\tilde{y}_s^2(\theta_b)\rangle_c^{p-1}}\frac{z^p}{p!}. \tag{26}$$

Note that the construction already satisfies the constraint equation $S_1 = S_2 = 1$. Now using the expressions for the higher moments of the SZ in terms of the matter power spectrum (see equation 15) gives

$$\tilde{\Phi}(z) \equiv \int_0^{r_s}\sum_{p=1}^{\infty}\frac{1}{p!}S_p\left[\frac{b_\pi^p(r)\omega_{\mathrm{SZ}}^p(r)}{d_A(r)^{2(p-1)}(r)}\frac{\mathcal{I}_{\theta_b}^{(p-1)}z^p}{\langle\tilde{y}_s^2(\theta_b)\rangle_c^{(p-1)}}\right]. \tag{27}$$

We can now use the definition of $\phi(z)$ for the matter cumulants to express $\tilde{\Phi}(z)$:

$$\tilde{\Phi}(z) = \int_0^{r_s}\mathrm{d}r\left[\frac{d_A^2(r)\langle\tilde{y}^2(\theta_b)\rangle_c}{\mathcal{I}_{\theta_b}}\right]\phi\left[b_\pi(r)\frac{\omega_{\mathrm{SZ}}(r)}{d_A^2(r)}\frac{\mathcal{I}_{\theta_b}}{\langle\tilde{y}_s^2(\theta_b)\rangle_c}z\right]. \tag{28}$$

---

[5] Equations (21) and (22) are crucial to any approach that uses the hierarchical ansatz for modelling of astrophysical phenomena including the results presented here. These equations were derived by Balian & Schaeffer (1989) as well as Bernardeau & Schaeffer (1992, 1999).

Note that we have used the fully non-linear generating function ϕ for the cumulants, though we will use it to construct a generating function in the quasi-linear regime. Next we relate these results to the statistics of previously defined quantity $\hat{y}_s$. For the reduced tSZ field $\hat{y}_s$, the cumulant generating function $\hat{\Phi}(z)$ is given by

$$\hat{\Phi}(z) = \sum_{p=1}^{\infty} \hat{S}_p \frac{z^p}{p!} = \frac{1}{\langle y(\theta_b) \rangle} \int_0^{r_s} dr \left[\frac{d_A^2(r)}{\langle y(\theta_b) \rangle_c} \frac{\langle \tilde{y}_s^2(\theta_b) \rangle_c}{\mathcal{I}_{\theta_b}} \right] \phi \left[b_\pi(r) \langle y(\theta_b) \rangle \frac{z}{\langle \tilde{y}_s^2(\theta_b) \rangle_c} \frac{w_{SZ}(r)}{d_A^2(r)} \mathcal{I}_{\theta_b} \right]. \tag{29}$$

The scaling function $\hat{h}(x)$ for $\hat{y}$ associated with the PDF $p(\hat{y})$ can now be related to the matter scaling function $h(x)$ using the following definition (Balian & Schaeffer 1989):

$$\hat{h}(x) = - \int_{-\infty}^{\infty} \frac{dz}{2\pi i} \exp(xz) \hat{\Phi}(z), \tag{30}$$

which takes the following form, using definitions corresponding to equation (23),

$$\hat{h}(x) = \int_0^{r_s} dr \frac{w_{SZ}(r) b_\pi(r)}{\langle y(\theta_b) \rangle} \left[\frac{d_A^2(r)}{\langle y(\theta_b) \rangle} \frac{\langle \tilde{y}_s^2(\theta_b) \rangle_c}{\mathcal{I}_{\theta_b} w_{SZ}(r) b_\pi(r)} \right]^2 h \left[x \frac{d_A^2(r)}{\mathcal{I}_{\theta_b} w_{SZ}(r) b_\pi(r)} \frac{\langle \tilde{y}_s^2(\theta_b) \rangle_c}{\langle y(\theta_b) \rangle} \right]. \tag{31}$$

While the expressions derived above are exact, and are derived for the most general case using only the small-angle approximation, they can be simplified considerably using further approximations. In the following we will assume that the contribution to the r integrals can be replaced by an average value coming from the maximum of $\omega_{SZ}(r)$, i.e. r_c ($0 < r_c < r_s$). So we replace $\int f(r) dr$ by $1/2 f(r_c) \Delta_r$, where Δ_r is the interval of integration and $f(r)$ is the function of comoving radial distance r under consideration. Similarly, we replace the $\omega_{SZ}(r)$ dependence in the l integrals by $\omega_{SZ}(r_c)$. Under these approximations, we can write

$$\hat{\Phi}(z) = \phi(z); \quad \hat{h}(x) = h(x). \tag{32}$$

Thus, we find that the statistics of the underlying field $1 + \delta$ and the statistics of the reduced field δy are exactly the same under such an approximation [the approximate functions $\hat{\Phi}(z)$ and $\hat{h}(x)$ do satisfy the proper normalization constraints]. Although it is possible to integrate the exact expressions of the scaling functions, there is some uncertainty involved in the actual determination of these functions and associated parameters that describes it from *N*-body simulations [e.g. see Munshi et al. (1999), Valageas, Lacey & Schaeffer (2000) and Colombi, Bouchet & Hernquist (1996) for a detailed description of the effect of the finite volume correction involved in their estimation].

In the following, we use $\hat{\Phi}(z)$ as derived above to compute $p(\delta \hat{y})$ with the help of equation (22). In addition to the generating function approach we have used the lognormal distribution as a model for the underlying statistics (see Appendix A for a detailed discussion on the lognormal distribution).

6.1 The bias associated with the tSZ sky

The bias for the underlying density field δ is defined using the joint two-point PDF $p(\delta_1, \delta_2)$ for density contrasts δ_1 and δ_2 measured at two different points separated by a fixed distance. Given the two-point correlation function ξ_{12} that characterizes the correlation hierarchy for this scale, the 2PDF $p(\delta_1, \delta_2)$ can be expressed in terms of the one-point PDFs and the bias functions $b(\delta)$ as follows:

$$p(\delta_1, \delta_2) = p(\delta_1) p(\delta_2) \left[1 + b(\delta_1) \xi_{12} b(\delta_2) \right]. \tag{33}$$

The bias function $b(\delta)$ is also useful in describing the bias associated with the overdense regions. Cumulant correlators are the lower order connected moments of the 2PDF $p(\delta_1, \delta_2)$.

To compute the bias associated with the peaks in the SZ field we have to first develop an analytic expression for the generating field $\tilde{\beta}(z_1, z_2)$ for the SZ field $\tilde{y}_s(\theta_b) = y_s(\theta_b) - \langle y(\theta_b) \rangle$. For that we will use the usual definition for the two-point cumulant correlator C_{pq} for the field:

$$\tilde{C}_{pq} = \frac{\langle \tilde{y}_s(\hat{\Omega}_1)^p \tilde{y}_s(\hat{\Omega}_2)^q \rangle_c}{\langle \tilde{y}_s^2(\theta_b) \rangle_c^{p+q-2} \langle \tilde{y}_s(\hat{\Omega}_1) \tilde{y}_s(\hat{\Omega}_2) \rangle_c}; \tag{34}$$

for a complete treatment of two-point statistical properties of smoothed fields, see Munshi et al. (1999b). We will show that, as is the case with its density field counterpart, the two-point generating function for the field y_s can also be expressed (under certain simplifying assumptions) as a product of two one-point generating functions, $\beta^{SZ}(z)$, which can then be directly related to the bias associated with 'hotspots' in y maps:

$$\hat{\beta}(z_1, z_2) = \sum_{p,q}^{\infty} \frac{\hat{C}_{pq}}{p! q!} z_1^p z_2^q = \sum_p^{\infty} \frac{\hat{C}_{p1}}{p!} z_1^p \sum_q^{\infty} \frac{\hat{C}_{q1}}{q!} z_2^q = \hat{\beta}(z_1) \hat{\beta}(y_2) \equiv \hat{\tau}(z_1) \hat{\tau}(z_2). \tag{35}$$

The tree structure of the correlation hierarchy that we have assumed is crucial to achieve the factorization derived above. It is also clear that the factorization of the generating function actually depends on the factorization property of the cumulant correlators, i.e. $\hat{C}_{pq} = \hat{C}_{p1} \hat{C}_{q1}$. Note that such a factorization is possible when the correlation of two patches in the directions $\hat{\Omega}_1$ and $\hat{\Omega}_2$ $\langle \tilde{y}_s(\hat{\Omega}_1) \tilde{y}_s(\hat{\Omega}_2) \rangle_c$ is smaller compared to the variance $\langle \tilde{y}_s^2(\theta_b) \rangle_c$ for the smoothed patches. The generating function $\tilde{\beta}(z_1, z_2)$ for $\tilde{C}_{pq}$ is constructed as follows:

$$\tilde{\beta}(z_1, z_2) = \sum_{p,q}^{\infty} \frac{\tilde{C}_{pq}}{p! q!} z_1^p z_2^q \equiv \sum_{p,q}^{\infty} \frac{1}{p! q!} \frac{z_1^p z_2^q}{\langle \tilde{y}_s^2(\theta_b) \rangle_c^{p+q-2}} \frac{\langle \tilde{y}_s(\hat{\Omega}_1)^p \tilde{y}_s(\hat{\Omega}_2)^q \rangle_c}{\langle \tilde{y}_s(\hat{\Omega}_1) \tilde{y}_s(\hat{\Omega}_2) \rangle_c}. \tag{36}$$

We will now use the integral expression for the cumulant correlators (Munshi et al. 1999a) in order to express the generating function which, in turn, uses the hierarchical *ansatz* and the far-field approximation as explained above. Using equation (19) we can write

$$\tilde{\beta}(z_1, z_2) = \sum_{p,q}^{\infty} \frac{\tilde{C}_{pq}}{p!q!} \frac{z_1^p}{\langle \tilde{y}_s^2(\theta_b)\rangle_c^{p-1}} \frac{z_2^q}{\langle y_s^2(\theta_b)\rangle_c^{q-1}} \frac{1}{\tilde{\xi}_{12}} \int_0^{r_s} dr \, d_A^2(r) b_\pi^{p+q}(r) \frac{\omega_{SZ}^p(r)\omega_{SZ}^q(r)}{d_A(r)^{2p} d_A(r)^{2q}} [\mathcal{I}_{\theta_b}]^{p+q-1} \mathcal{I}_{\theta_{12}}; \tag{37}$$

$$\tilde{\xi}_{12} = \langle \tilde{y}_s(\hat{\Omega}_1)\tilde{y}_s(\hat{\Omega}_2)\rangle. \tag{38}$$

It is possible to further simplify the above expression by separating the summation over dummy variables p and q, which will be useful to establish the factorization property of the two-point generating function for bias $\hat{\beta}(z_1, z_2)$. We can now decompose the double sum over the two indices into two separate sums over individual indices. The above expression is quite general and depends only on the small-angle approximation and the large-separation approximation and is valid for any given specific model for the generating function $\mathcal{G}(\tau)$. However, it is easy to notice that the projection effects as encoded in the line-of-sight integration do not allow us to write down the two-point generating function $\hat{\beta}(z_1, z_2)$ simply as a product of two one-point generating functions $\hat{\beta}(z)$ as was the case for the density field $1 + \delta$. As in the case of the derivation of the PDF it simplifies matters if we use the reduced smoothed tSZ field $\hat{y}_s$. The statistical properties of $\hat{y}_s$ are very similar to that of the underlying 3D density field (under certain simplifying approximations) and are roughly independent of the background geometry and dynamics of the universe,

$$\hat{\beta}(z_1, z_2) = \int_0^{r_s} dr \frac{1}{\langle y(\theta_b)\rangle^2} d_A^2(r) \frac{\mathcal{I}_{\theta_{12}}}{\tilde{\xi}_{12}} \frac{\langle \tilde{y}_s^2(\theta_b)\rangle_c}{\mathcal{I}_{\theta_b}} \hat{\beta}\left(b_\pi(r)\langle y\rangle \frac{z_1}{\langle \tilde{y}_s^2(\theta_b)\rangle_c} \frac{\omega_{SZ}(r)}{d_A^2(r)} \mathcal{I}_{\theta_b}\right) \frac{\langle \hat{y}_s^2(\theta_b)\rangle_c}{\mathcal{I}_{\theta_b}} \hat{\beta}\left(b_\pi(r)\langle y\rangle \frac{z_2}{\langle \tilde{y}_s^2(\theta_b)\rangle_c} \frac{\omega_{SZ}(r)}{d_A^2(r)} \mathcal{I}_{\theta_b}\right). \tag{39}$$

While the above expression is indeed very accurate and relates the generating function of the density field to that of the tSZ field, it is difficult to handle in practice. Also it is important to note that the scaling functions such as $h(x)$ for the density PDF and $b(x)$ for the bias associated with overdense objects are typically estimated from numerical simulations specially in the highly non-linear regime. Such estimations are plagued with several uncertainties such as finite size of the simulation box. It was noted in earlier studies that such uncertainties lead to only a rather approximate estimation of $h(x)$. The estimation of the scaling function associated with the bias, i.e. $b(x)$ (here $x = (1 + \delta)/\bar{\xi}_\delta^{(2)}$), is even more complicated due to the fact that the two-point quantities such as the cumulant correlators and the bias are more affected by finite size of the catalogues. So it is not fruitful to actually integrate the exact integral expression we have derived above and we will replace all line-of-sight integrals with their approximate values. Following our construction of the one-point PDF or $p(\delta)$ we will replace integrals such as $\int_0^{r_s} f(r) \, dr$ with their approximate values $\int_0^{r_s} f(r) \, dr = 1/2 f(r_c)\Delta r$; r_c is at an intermediate redshift along the line of sight, its exact value is not important as the final result will be independent of r_c. For more accurate results we can Taylor expand $f(r)$ or integrate the exact expression:

$$\langle y_s(\theta_b)\rangle \approx \frac{1}{2} r_s b_\pi(r_c)\omega_{SZ}(r_c), \qquad \langle \tilde{y}_s^2(\theta_b)\rangle_c \approx \frac{1}{2} r_s \frac{\omega_{SZ}^2(r_c)}{d_A^2(r_c)} b_\pi^2(r_c)\left[\int \frac{d^2l}{(2\pi)^2} P_\delta\left(\frac{l}{d_A(r_c)}\right) b_l^2(\theta_b)\right], \tag{40}$$

$$\langle \tilde{y}_s(\hat{\Omega}_1)\tilde{y}_s(\hat{\Omega}_2)\rangle_c \approx \frac{1}{2} r_s \frac{\omega_{SZ}^2(r_c)}{d^2(r_c)} b_\pi^2(r_c)\left[\int \frac{d^2l}{(2\pi)^2} P_\delta\left(\frac{l}{d_A(r_c)}\right) b_l^2(\theta_b) \exp[i\, \mathbf{l}\cdot\theta_{12}]\right]. \tag{41}$$

Use of these approximations gives us the leading-order contributions to these integrals and we can check that to this order we recover the factorization property of the generating function, i.e. $\hat{\beta}(z_1, z_2) = \hat{\beta}(z_1)\hat{\beta}(z_2) = \beta(z_1)\beta(z_2) \equiv \hat{\tau}(z_1)\hat{\tau}(z_2)$. So it is clear that at this level of approximation, due to the factorization property of the cumulant correlators, the bias function $\hat{b}(x)$ associated with the peaks in the field $\hat{y}_s$, beyond certain threshold, obeys a similar factorization property too, which is exactly the same as its density field counterpart. Earlier studies have established such a correspondence between the weak-lensing convergence and the underlying density field in the case of one-point and two-point PDF $p(\delta)$ (Munshi & Jain 1999b),

$$\hat{b}(x_1)\hat{h}(x_1)\hat{b}(x_2)\hat{h}(x_2) = b(x_1)h(x_1)b(x_2)h(x_2). \tag{42}$$

Here we have used the following relation between $\hat{\beta}(z) = \tau(z)$ and $\hat{b}(x)$,

$$\hat{b}(x)\hat{h}(x) = -\frac{1}{2\pi i} \int_{-i\infty}^{i\infty} dz \, \hat{\tau}(z) \, \exp(xz). \tag{43}$$

In equation (32) we have already proved that $\hat{h}(x) = h(x)$; hence, from equation (42) we deduce that $\hat{b}(x) = b(x)$. This means that the bias associated with $\delta\hat{y}$ is identical to that of the underlying density contrast δ. This is one of the main results of this paper. For all practical purposes, we found that the differential bias as defined above is lot more difficult to measure from numerical simulations as compared to its integral counterpart where we concentrate on the bias associated with peaks above certain threshold,

$$\hat{b}(>x)\hat{h}(>x) = -\frac{1}{2\pi i} \int_{-i\infty}^{i\infty} dz \, \frac{\hat{\tau}(z)}{z} \exp(xz). \tag{44}$$

It is important to note that although the bias $\hat{b}(x)$ associated with the tSZ field $\hat{y}_s$ and the underlying density field are the same, the variance associated with the density field is very high but the projection effects in the tSZ field bring down the variance to a value comparable to unity.

This indicates that we can use the integral definition of bias to recover it from its generating function [see equations (43) and (44)]. Now, writing down the full two-point PDF for two correlated spots in terms of the tSZ field $\hat{y}_s(\theta_b)$:

$$p(\hat{y}_1, \hat{y}_2)d\hat{y}_1 d\hat{y}_2 = p(\hat{y}_1)p(\hat{y}_2)(1 + b(\hat{y}_1)\xi_\delta^{(2)}(r_1, r_2)b(\hat{y}_2))d\hat{y}_1 d\hat{y}_2; \qquad \hat{y}_i \equiv \hat{y}_s(\hat{\Omega}_i). \tag{45}$$

The results derived here for autocorrelation can be generalized to cross-correlation analysis; this extension will be presented elsewhere. It is important to realize that the bias $b(\hat{y}_s)$ is related to the bias of 'hotspots' in the tSZ map and relates their distribution with the overall correlation structure of the tSZ maps. The bias b_π defined earlier, on the other hand, relates the 3D pressure distribution $\pi_e(\boldsymbol{x})$ to the underlying density distribution $\delta(\boldsymbol{x})$.

7 SIMULATIONS

Two main approaches are generally used to simulate tSZ maps: (i) semi-analytical methods; (ii) direct numerical simulations. In the following we discuss maps made using both sets of techniques.

7.1 Simulations generated using semi-analytical methods

The semi-analytical methods identify clusters from purely collisionless or *N*-body simulations; simplifying assumptions regarding the distribution, hydrodynamical and thermodynamic equilibrium properties of the baryons are then used to create a baryonic data cube from the underlying dark matter distribution. The resulting distribution of baryons is then eventually used to create tSZ *y* maps. This method was pioneered by Kay, Liddle & Thomas (2001) and was later used by Schulz & White (2003) and White (2003). In our study we have made use of data described in White (2003), where more detailed discussion about these simulations as well as the process of generating the tSZ *y* maps that we have used can be found.[6] The numerical simulations are rather expensive and semi-analytical methods can provide reasonably accurate results that can be used to understand the underlying physical processes which affect the statistics of tSZ process. The particular cosmology that we will adopt for numerical study is specified by the following parameter values : $\Omega_\Lambda = 0.741$, $h = 0.72$, $\Omega_b = 0.044$, $\Omega_{CDM} = 0.215$, $n_s = 0.964$, $\sigma_8 = 0.803$.

7.2 Hydrodynamic simulations

Early simulations of the tSZ modelled gravitational collapse and adiabatic compression but initially ignored the effect of adiabatic cooling which affects the thermal state of the gas especially in the haloes. It was soon realized, however, that the baryons are subjected to non-gravitational heating processes – such as the feedback of energy from SN or AGN. Over the years the field of numerical simulations has matured to such an extent that it is now possible to include these effects self-consistently and in a reasonably large simulation box.

The simulated *y* maps that we have used were generated by Scott et al. (2012) using Millennium Gas Simulations (Hartley et al. 2008; Starek, Rudd & Evrard 2009; Short et al. 2010; Young et al. 2011), which in turn were generated to provide hydrodynamic versions of the Virgo Consortium's dark matter Millennium Simulations and were performed using the publicly available GADGET2 *N*-body/hydrodynamics code (Springel 2005). Two different versions of the simulations use the same initial conditions and box size. In the first run, the gas was modelled as ideal non-radiative fluid and was allowed to undergo adiabatic changes in regions of non-zero pressure gradient. The evolution was modelled using smoothed particle hydrodynamics (SPH). An artificial viscosity too was used to convert bulk kinetic energy of the gas into its internal energy. This is essential to capture the physics of shock and thus generate quasi-hydrostatic equilibrium. This process ensures quasi-hydrostatic equilibrium inside vitalized haloes. See the text for more details of the hydrodynamic simulations used to generate these maps. These sets of simulations will be referred to as GO simulations. Non-radiative descriptions of intercluster gas do not reproduce the observed X-ray properties of the clusters (Voit 2005). So the next set of simulations that we use model preheated gas at high redshift that can generate the required core entropy and capable of producing a steeper X-ray luminosity–temperature relation in agreement with observations. The entropy level of the second set of simulations was chosen to match the mean X-ray luminosity–temperature relation at $z = 0$ (Edward & Henry 1991; Kaiser 1991). These simulations also include radiative cooling and an entropy sink. We will refer to these simulations as PC. Cooling in these simulations does not play an important role as the cooling time for the preheated gas is long compared to the Hubble time. The cosmological parameters of these simulations are $\Omega_{CDM} = 0.25$, $\Omega_\Lambda = 0.75$, $\Omega_b = 0.045$, $h = 0.73$ and $\sigma_8 = 0.9$.

The scaled $\log_{10}[y/\langle y \rangle]$ parameter distribution of a realization is shown in Fig. 6 for GO simulations and in Fig. 7 for simulations with preheating and cooling (PC). The left-hand panels show contribution from all individual components. The middle panels represent contribution from overdense regions that satisfy the constraint $1 + \delta < 100$. Finally, the right-hand panels correspond to the contribution to the *y* map from gas which satisfies the constraint $T < 10^5$ K.

There is a very clear and obvious difference between the two sets of maps in that the GO maps have more substructure. The smoothness of the PC maps is due to the external thermal energy added to the gas by the preheating process. The mean *y* parameter in the GO simulations is $\langle y \rangle = 2.3 \times 10^{-6}$ and in the PC simulations it is nearly four times higher $\langle y \rangle = 9.9 \times 10^{-6}$. These values are consistent with the *COBE*/Far Infrared Absolute Spectrophotometer constraint $\langle y \rangle \leq 1.5 \times 10^{-5}$. However, it is believed that such a high level of preheating would definitely

---

[6] http://mwhite.berkeley.edu/tSZ/

remove some of the absorption features seen in the Lyman α spectrum observed towards quasars (Theuns, Mo & Schaye 2001; Shang, Crotts & Haiman 2007; Borgani & Viel 2009). Indeed, the PC model studied here should be treated as an *extreme test* of the effect of a high-preheating scenario.

In terms of source contributions, the bulk of the y signal comes from low redshift, i.e. $z < 2$. However, in case of PC simulations the opposite is true, where 80 per cent of the signal originates from $z < 3.5$. The overdense regions such as the group or clusters are the sources of y signal in the GO simulations which are primarily embedded in structures that collapsed at relatively lower redshift. In case of the PC simulations, most of the signals comes from mildly overdense gas at high redshift. It is interesting to notice that the GO simulations do get contributions from the gas at high redshift, $z > 4$. However, such contributions are completely erased in the case of the PC simulations. This is primarily due to the fact that radiative cooling erases most of the ionized gas at these redshifts.

8 TESTS AGAINST NUMERICAL SIMULATIONS

In this section we present the result of our comparison of theory against the simulations described in the previous section. We have checked our results against simulations that are based on N-body simulations where baryon is added using a semi-analytical prescription. We have also compared our results against the state-of-the-art hydrodynamic simulations.

8.1 Semi-analytic simulations

We have used simulated y maps described in White (2003) to test our theoretical predictions. The simulations were generated on a 1024×1024 grid and cover $10° \times 10°$ patches on the surface of the sky. To compute the PDF and the bias we construct the reduced $\hat{y}_s$ maps from the beam-smoothed y_s. A Gaussian beam with varying FWHM $\theta_b = 30$ arcsec, 1 arcmin, 5 arcmin, 10 arcmin was used for this purpose. The binning of the data at each grid point was next performed to the histogram and finally the one-point PDF of $\hat{y}_s$. In Fig. 3 we have presented the results of our calculations for the entire range of beam sizes and compared them against the results from the simulations.

For computation of the bias $b(\hat{y}_s)$ from the precomputed $\hat{y}_s$ we found that the estimation of cumulative bias $b(> \hat{y}_s)$ is much more stable than its differential counterpart $b(\hat{y}_s)$. We used the following expression for computation of the bias function:

$$b(> \hat{y}_s) = \frac{1}{\sqrt{\langle \hat{y}_1 \hat{y}_2 \rangle}} \left[\frac{\int_{\hat{y}_s}^{\infty} d\hat{y}_1 \int_{\hat{y}_s}^{\infty} d\hat{y}_2 \, p(\hat{y}_1, \hat{y}_2)}{[\int_{\hat{y}_s}^{\infty} dy_1 \, p(\hat{y}_1)]^2} - 1 \right]. \tag{46}$$

The one-point and two-point PDFs as well as the two-point correlation function are all constructed at grid points. We found the numerical computation of $b(> \hat{y}_s)$ to be much more stable than that of the differential bias $b(\hat{y}_s)$. The computation of two-point PDFs was done using different separation angular scales θ_{12}. The theoretical bias is computed at the large-separation limit. However, we found that this limit is reached very quickly, typically at an angular scale which is twice the FWHM, i.e. $\theta_{12} \sim 2\theta_0$. We also notice that the estimation of the bias is independent of any assumption regarding the factorizability of 2PDF, i.e. equation (46) does not depend on any such ad hoc assumptions.

In Fig. 4 we have shown the integrated bias $b(> \hat{y}_s)$ computed using two different analytical techniques as a function of the threshold y_s. In the right-hand panel the various smoothing angular scale FWHM we have shown correspond to $\theta_b = 30$ arcsec, 1 arcmin, 5 arcmin, 10 arcmin. The solid lines correspond to the numerical simulations. The dashed lines correspond to predictions from the lognormal model. This bias for higher $\hat{y}_s$ regions is higher. The results for the perturbative calculations are shown only for $\theta_b = 10, 5$ arcmin. For smaller beam the perturbative calculations break down.
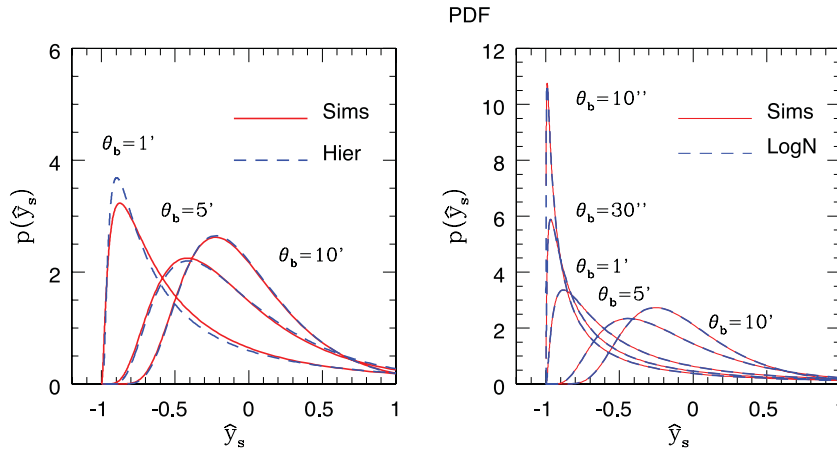

Figure 3. The PDF $p(\hat{y}_s)$ is plotted as a function of $\hat{y}_s$. Various curves correspond to different beam sizes (FWHM) as indicated. Two different analytical models are shown; the lognormal (right-hand panel) and the hierarchical ansatz (left-hand panel). The solid lines correspond to the results from numerical simulations. The dashed lines in each panel represent the analytical results.
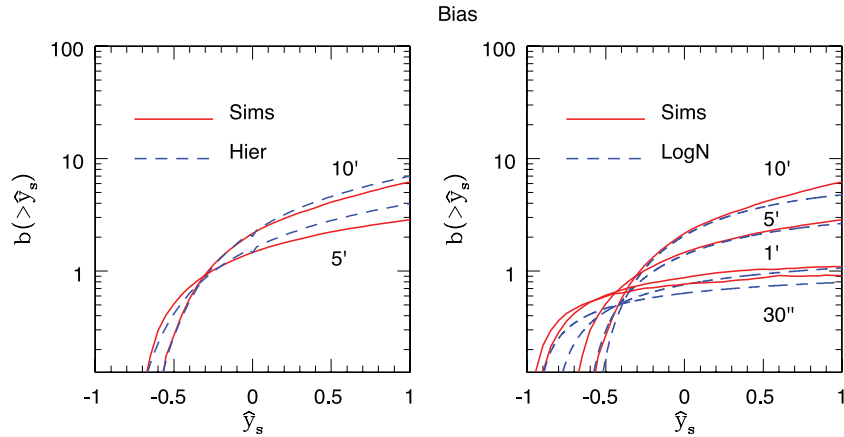
Figure 4. The cumulative bias associated with $b(> \hat{y}_s)$ is plotted as a function of $\hat{y}_s$. Various curves correspond to different beam sizes (FWHM) as indicated. Two different analytical models are shown; the lognormal (right-hand panel) and the hierarchical ansatz (left-hand panel). The solid lines correspond to the results from numerical simulations. The dashed lines in each panel represent the analytical results.
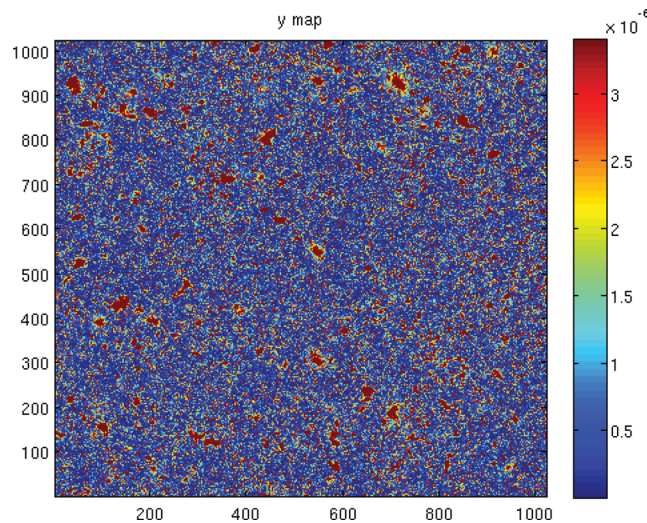
Figure 5. A simulated map of y sky used in our study. The maps are $10°$ on a side and were generated on a 1024×1024 grid. These simulations were made using semi-analytical methods developed by Schulz & White (2003). More details about the simulations can be found in White (2003).
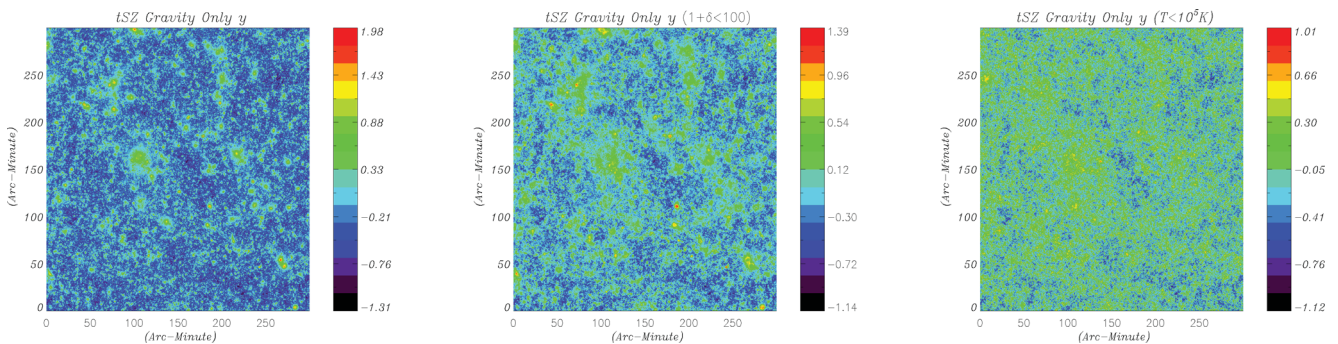
Figure 6. Simulated $5° \times 5°$ dimensionless scaled tSZ maps $\log_{10}[y/\langle y \rangle]$ are depicted. The maps were generated using the Virgo Consortium's Millennium Gas Simulation. The left-hand panel shows the resulting y maps. The middle panel corresponds to maps generated using low-density regions. Only overdense regions with density $1 + \delta < 100$ were considered. The right-hand panel corresponds to low-temperature regions $T < 10^5$ K. These sets of hydrodynamic simulations ignore preheating but take into account adiabatic cooling. We will refer to them as GO simulations (see the text for more details).
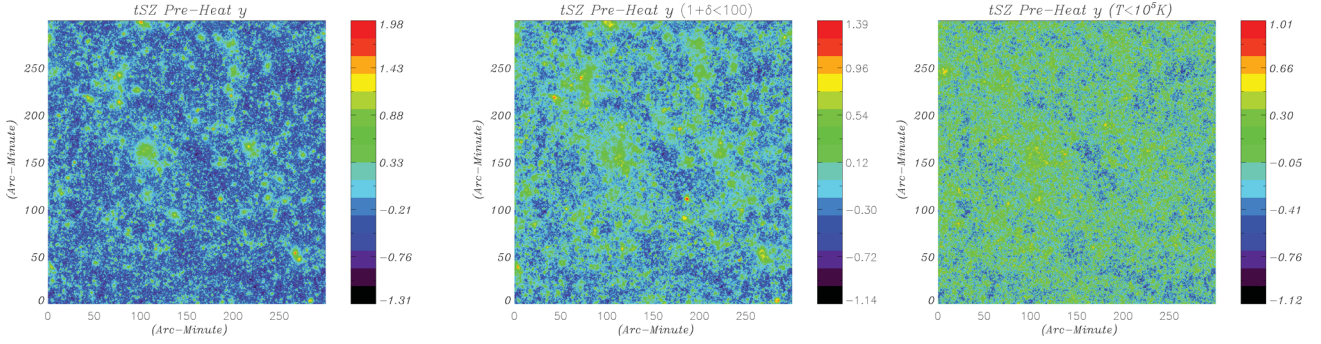
Figure 7. Same as the previous figure, but for simulations with preheating and cooling. These simulations will be referred to as PC simulations.

By construction, the statistics of the $\hat{y}$ field are insensitive to the background cosmology in that they mimic the statistics of the underlying density contrast δ. Hence, the shape of its PDFs does not depend on the detailed modelling of the electron pressure π_e or the related electron pressure bias $b_\pi(r)$. The variance of these distributions however does depend on this function. We have used the variance $\langle \hat{y}_s^2 \rangle_c$ computed from the maps in our computation of the PDFs. In Fig. 5 a $10° \times 10°$ map, generated using semi-analytical methods, is shown.

8.2 Hydrodynamical (SPH) simulations

In addition to the maps generated using semi-analytical methods, we have also used maps generated by realistic state-of-the-art hydrodynamic simulations. These maps are $5° \times 5°$ in size and are constructed using a 1024×1024 grid. We have analysed two different sets of maps to test our analytical predictions which we describe below.

8.2.1 Simulations with adiabatic cooling

The first set of maps are derived from the GO simulations described previously. To these we have compared both the lognormal approximation and the predictions from analytical results of Valageas & Munshi (2004). We have tried three different angular scales $\theta_b = 15$ arcsec, 1.25 arcmin, 2.5 arcmin, respectively. We numerically evaluate the statistics of $\hat{y}_s$, using exactly the same technique described before. We find that the results from numerical simulations are reproduced extremely well in the realistic and up-to-date hydrodynamic simulations. In the case of the GO simulations, where gravitational dynamics and adiabatic cooling are the main factors influencing structure formation, the numerical PDF is reasonably reproduced by theoretical predictions. We have presented these results in Fig. 8. As noted before, perturbative predictions start to break down when the variance at a given scale reaches unity. The theoretical predictions of Valageas & Munshi (2004) remedy the situation and are useful for analytical prediction of PDF at an arbitrary non-linear scale. We find that analytical prediction for $\hat{y}_s$ is accurate down to very low values of PDF. It reinforces our conclusions drawn from the analysis of maps generated using semi-analytical techniques. Though the maps from hydrodynamical simulations have less sky coverage compared to the semi-analytical maps used before, they have more realistic representation of the baryonic physics responsible for the tSZ effect.
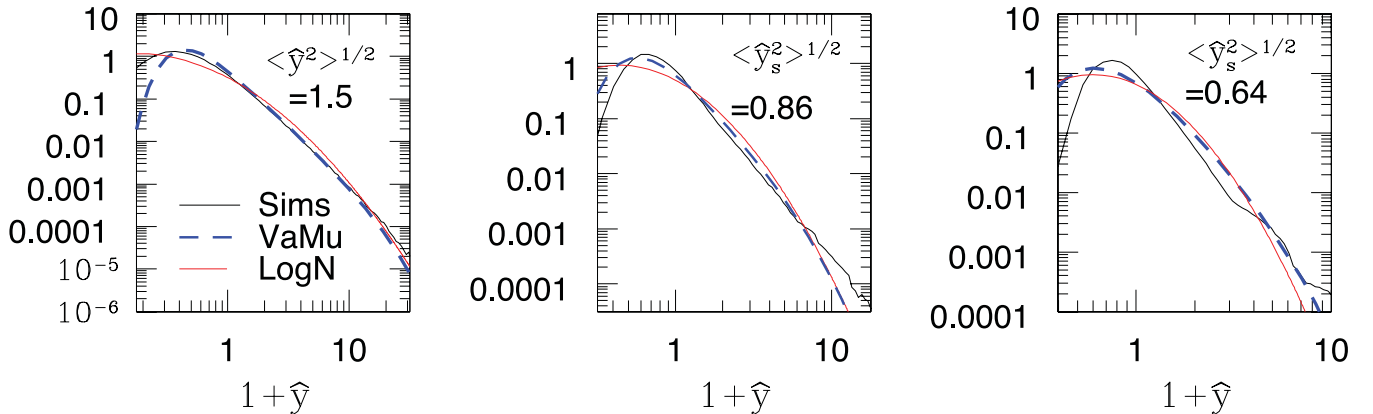

Figure 8. The PDF for $\hat{y}$ is being compared to theoretical predictions from the lognormal distribution and an extension of the hierarchical model as proposed by Valageas & Munshi (2004). The black solid lines represent the PDF computed from the simulation. The red solid and blue dashed lines correspond to the lognormal model and the hierarchical model of Valageas & Munshi (2004). The smoothing angular scales correspond to $\theta_0 = 0.25$ arcsec (left-hand panel), $\theta_0 = 1.25$ arcmin (middle panel) and $\theta_0 = 2.5$ arcmin, respectively. The numerical curves are averages of three individual realizations each.

In addition to studying the $\hat{y}_s$ maps, we have divided the entire contribution from various baryonic components to check how our theoretical prescriptions compare with that from simulations for individual components. In this context, we notice that thermodynamic states of baryons, as well as their clustering, at low-to-medium redshift $z < 5$ have been studied, using both numerical and analytical techniques. In their studies, Valageas et al. (2002) have used the hierarchical ansatz to study the *phase diagrams* of cosmological baryons as a function of redshift. The low-temperature 'cool' component of the IGM represented by Lyman α forest typically satisfies the constrain $10^3 < T < 10^4$ K. The exact values of the lower and upper limit depend somewhat on the redshift. The 'cold' component of the IGM is very well characterized by a well-defined equation of state. The 'warm' component of the IGM on the other hand is shock-heated to a temperature range of $10^4 < T < 10^7$ K due to the collapse of non-linear structure and cannot be defined by a well-defined equation of state. Though the 'warm' component does follow a mean temperature–density relation, the scatter around this relation however is more significant than for the 'cool' component. Both the 'cool' and 'warm' components originate outside the collapsed haloes and typically reside in moderate overdensites $1 + \delta < 100$. Finally, the remaining contribution comes from the hot baryonic component of the virialized high-density haloes with temperatures $T > 10^7$ K.

In Fig. 9 we have compared the contributions from the medium-overdensity regions $1 + \delta < 100$ (medium panel) which are caused by both the 'warm' and 'cool' components of the IGM. The right-hand panel corresponds to emission primarily from the 'cool' component. The variance corresponding to these individual components is computed individually and used as an input in the computation of their PDF. The results are presented for the particular case of smoothing $\theta_s = 15$ arcsec although the agreement is equally good for other smoothing angular scale. The sharp drops seen in the PDFs are due to the finite size of the catalogue. The lowest probability that we can compute using a 1024×1024 grid is roughly 10^{-6}. For larger smoothing angular scales, it is slightly less. In Fig. 10 we have shown cumulative bias associated with $\hat{y}$ for various smoothing angular scales.

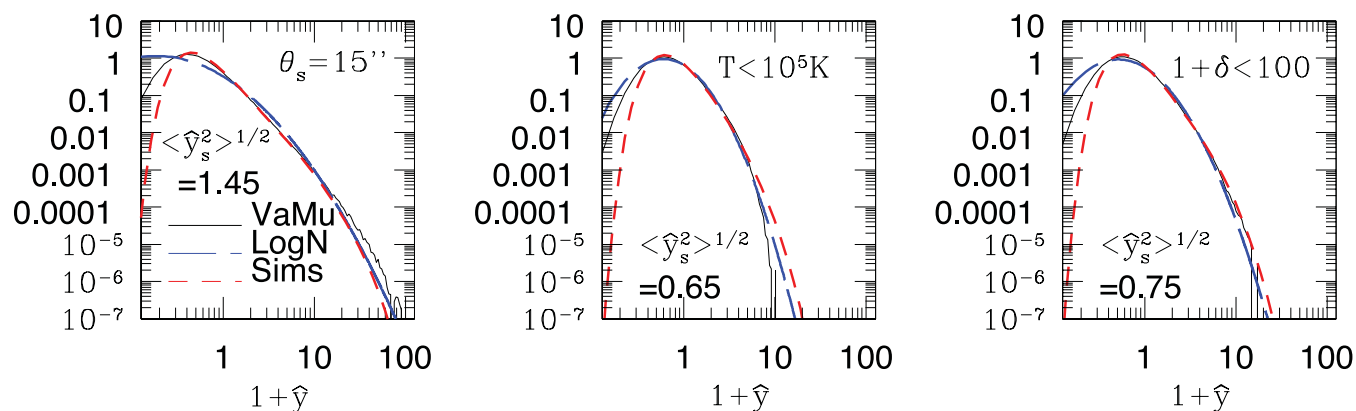## Gravity and Adiabatic Cooling Simulations: PDF

Figure 9. The PDF for $\hat{y}$ is being compared to theoretical predictions from the lognormal distribution and an extension of the hierarchical model as proposed by Valageas & Munshi (2004). The black solid line represents the PDF computed from the simulation. The blue dashed and red dashed lines correspond to the lognormal model and the hierarchical model of Valageas & Munshi (2004). The smoothing angular scales correspond to $\theta_0 = 0.25$ arcsec (left-hand panel), $\theta_0 = 1.25$ arcmin (middle panel) and $\theta_0 = 2.5$ arcmin (right-hand panel), respectively. The numerical curves are averages of three individual realizations each.
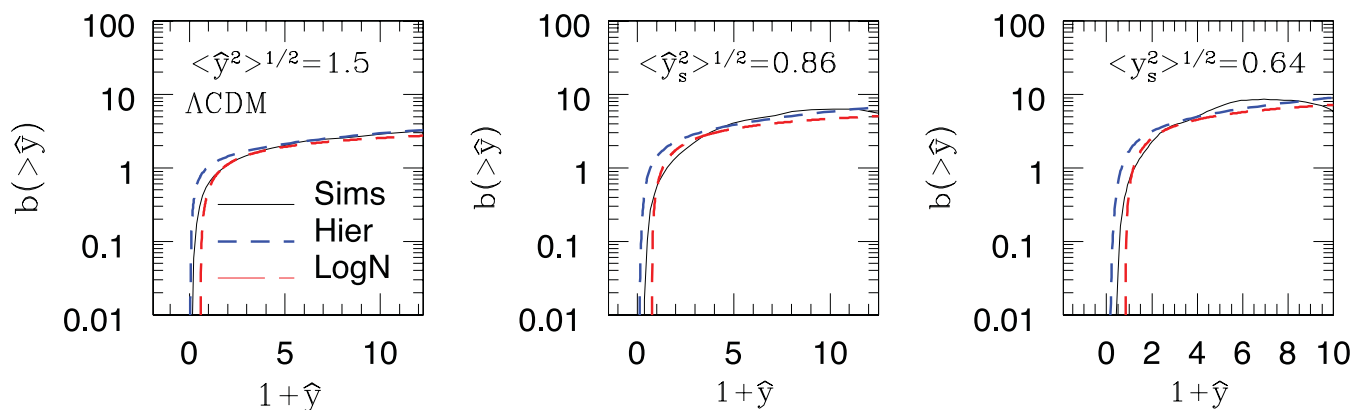
Gravity and Adiabatic Cooling Simulations : Bias

Figure 10. The bias $b(> y_s)$ plotted as a function of y_s for various smoothing angular scales corresponding to $\theta_0 = 0.25$ arcsec (left-hand panel), $\theta_0 = 1.25$ arcmin (middle panel) and $\theta_0 = 2.5$ arcmin (right-hand panel). Theoretical predictions from hierarchical ansatz (short dashed), lognormal (long dashed) and simulations (solid lines) are shown.
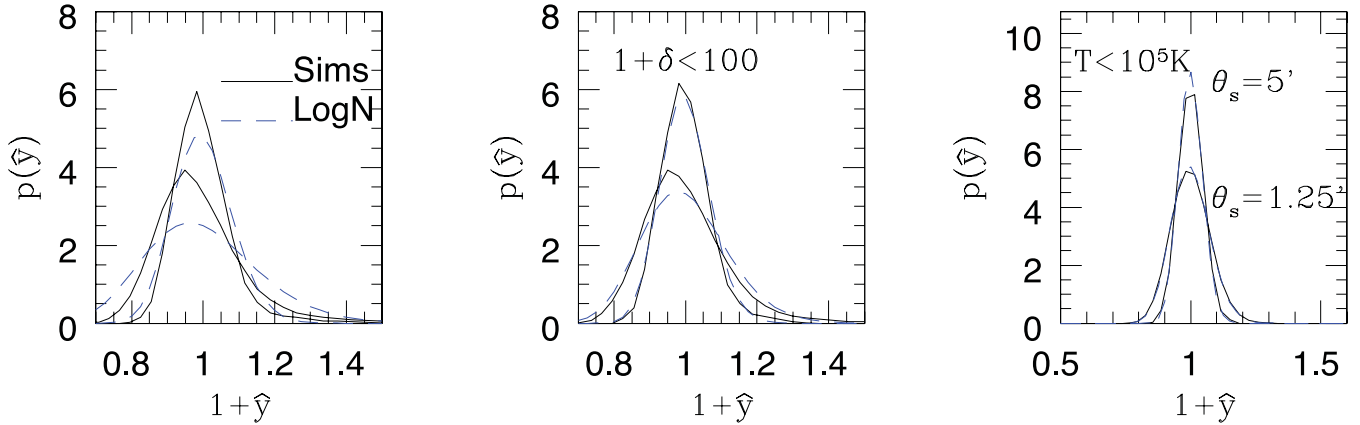
Pre-Heating Simulations : PDF

Figure 11. The PDF $p(\hat{y})$ of $\hat{y}$ is compared to theoretical predictions from the lognormal distribution and an extension of the hierarchical model as proposed by Valageas & Munshi (2004). From left to right panels correspond to total contribution, contribution from regions of low overdensity $1 + \delta < 100$ as well as contribution only from low-temperature regions $T < 10^5$ K of the simulations. In each panel we show two smoothing scales $\theta_s = 1.25$ arcmin and $\theta_s = 5$ arcmin, respectively.

The computation of integrated bias $b(> y_s)$ was carried out using techniques discussed in the previous section. We find that the analytical predictions for bias match very accurately with the one recovered from numerical simulations. These results are presented in Fig. 4. The bias were estimated for the same angular scale. Indeed, in almost all cases the predictions for the lognormal as well as hierarchical models are very close. An extension of the Valageas & Munshi (2004) technique for the case of bias is possible, but has not been worked out. However, bias computed using the hierarchical model and lognormal approximation seems to be reasonably accurate. The bias $b(>y_s)$ being a two-point statistic is more sensitive to sample variance.

8.2.2 Simulations with adiabatic cooling and preheating

The second set of simulations that we have analysed includes preheating and is referred to as the PC simulations. The smoothness of the PC maps is reflected in their low variance. This is primarily due to the high level of the preheating that erases many substructures resulting in maps with less features. We include these simulations in our studies mainly to test the limitations of analytical predictions. The fundamental assumption in our analytical modelling is of gravity-induced structure formation where baryons are considered as the biased tracers of underlying dark matter clustering. We find the significant deviation of the numerical results from theoretical predictions in the presence of high-level preheating at small angular scales (Fig. 11). These deviations are more pronounced at smaller angular scales. The PDFs become Gaussian at scales $\theta_s \sim 10$ arcmin or larger. The deviation at all scales is less pronounced if we remove the collapsed objects and focus on the maps with overdensites $1 + \delta < 100$. However, the PDF of the y distribution from 'cold' intergalactic gas is represented very accurately by our analytical results at all angular scales in the presence of preheating (Fig. 12).

9 CONCLUSIONS

We have studied the prospects for extracting and using the non-Gaussian statistical signatures from tSZ maps. The tSZ effect is associated with the hot gas in large-scale structure that is probed by multifrequency CMB experiments. When compared to the CMB temperature anisotropies, the tSZ effect has a distinct spectral dependence with a null at a frequency of 217 GHz. This distinct spectral signature of the SZ effect means it can be effectively separated from the primary CMB contributions. This will provide a unique opportunity to probe the tSZ effect using data from ongoing surveys.

The statistical analysis of frequency-separated tSZ maps has so far been mainly focused on lower order statistics or topological descriptors (Munshi et al. 2012). Non-Gaussianity in the tSZ signal is additional information that is useful in constraining the large-scale pressure fluctuation associated with the tSZ effect. This signature can be useful for constraining non-gravitational effects such as preheating or other forms of energy injection in the form of feedback from AGN or SN.

The tSZ effect traces the pressure fluctuations associated with the large-scale distribution of the baryonic gas. The pressure fluctuations due to the virialized dark matter haloes can be modelled by assuming them to be in hydrostatic equilibrium with the dark matter distribution in the halo. Such a halo model description has been extensively used in understanding the statistical properties of the tSZ effect as well as other CMB secondaries (Cooray & Seth 2002).

In addition to the halo model prescription, a redshift-dependent linear biasing scheme that relies on a perturbative description of dark matter clustering has also been in use to model certain aspects of the tSZ effect. It was introduced by Goldberg & Spergel (1999a,b).
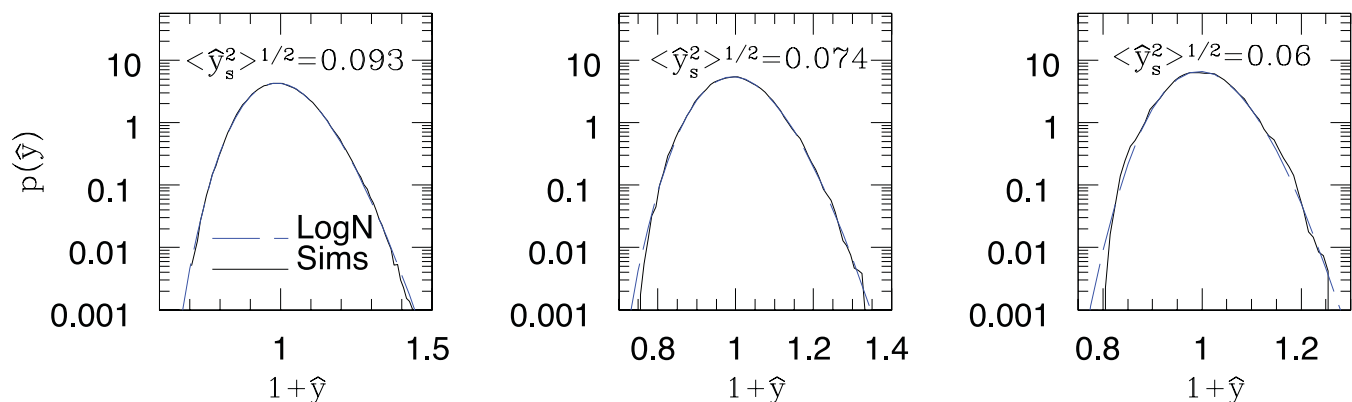
T<10⁵K systems in Pre−Heating Simulations: PDF

Figure 12. The PDF for $\hat{y}$, $p(\hat{y})$, from numerical simulations (solid lines) for 'cold' $T < 10^5$ K components are compared against the theoretical predictions from the lognormal distribution (dashed lines). The hierarchical model as proposed by Valageas & Munshi (2004) produces nearly identical results and are not shown. The angular scales considered from left to right are $\theta_s = 0.25$ arcsec, $\theta_s = 1.25$ arcmin and $\theta_s = 2.5$ arcmin, respectively.

Combining such a model with prescriptions from HEPT of Scoccimarro & Frieman (1999) can be used to predict the lower order moments; this approach has been tested successfully against numerical simulations by Cooray, Hu & Tegmark (2000).

In the following we summarize the main conclusions of this study.

Use of perturbative approach and its extension by Valageas & Munshi (2004). We have used the approach developed by Goldberg & Spergel (1999a,b) and Cooray et al. (2000) to construct the PDF and bias. We construct the entire cumulant-generating function and show that under certain simplifying assumptions it becomes independent of the details of the biasing scheme. The generating function adopted here was developed primarily for the construction of 3D and 2D (projected) density distributions that are studied using galaxy surveys; later it was used in construction of the weak-lensing PDF in small and large smoothing angular scales. In this paper we have shown that a similar technique can be adopted for the study of tSZ when it is expressed in terms of the 3D pressure fluctuations. We have compared these results against two sets of maps: (a) maps made from semi-analytical simulations which are of $10^\circ \times 10^\circ$ in size (b) $5^\circ \times 5^\circ$ maps using full SPH simulations (the Millennium Gas Simulations from the Virgo Consortium). We have studied angular scales $10\,\text{arcsec} < \theta_b < 10\,\text{arcmin}$ for the semi-analytical maps and $2.5\,\text{arcsec} < \theta_b < 5\,\text{arcmin}$ for the smaller maps. On angular scales where the rms fluctuation in y_s maps is lower than unity, the perturbative series is valid and the analytical predictions are in very good agreement with numerical simulations; we find analytical results from perturbation theory to be accurate for angular scales larger than a few arcminutes ($\theta_b > 2\,\text{arcmin}$). As a result of our study, we notice that even at comparatively large angular scales, $\theta_b > 10\,\text{arcmin}$, the PDF distribution of the tSZ effect is highly non-Gaussian. Going beyond the perturbative approach, we have used the formalism presented in Valageas & Munshi (2004) to extend the analytical predictions to all angular scales. We find excellent agreement with theory and simulations for all possible angular scales studied by us for simulation where gravity and adiabatic cooling play a dominant role.

Use of lognormal approximation. In addition to the perturbative approach and its extension using hierarchical *ansatz*, we have also used a model based on the lognormal distribution. The lognormal model is non-perturbative and has been used widely in the literature. Like the perturbative approach it has been used to model the results from galaxy surveys (Hamilton 1985; Coles & Jones 1991; Bouchet et al. 1993; Kofman et al. 1994), weak-lensing observables (Munshi 2000; Taruya et al. 2002) as well as Lyman α statistics (Bi & Davidson 1997). The validity of the lognormal model has been compared against numerical simulations as well as against perturbative or hierarchical methods (Bernardeau & Kofman 1995). In the entire range of angular scales considered by us, we find the lognormal model to be a very good approximation for the $\hat{y}$ parameter distribution. We have also used the bias computed from the lognormal approximation and found it to be in reasonable agreement.

Isolating the effect of background cosmology. We have shown that the statistics of $\hat{y}$ can be described using analytical models of gravitational clustering alone, and the S_N parameters that describe the PDF as well as the entire PDF are insensitive to the background cosmology – the lognormal model, e.g., does not have any cosmology built into it. The power spectrum of y on the other hand is sensitive to the amplitude of the density fluctuations, σ_8 and other cosmological parameters. Using higher order statistics, such as the skewness, previous authors argued the possibility of separation of the pressure bias from the amplitude of the density fluctuations (Hill & Sherwin 2012). The dimensionless parameter $\hat{y}$ that we have introduced here is insensitive to background cosmology and in this sense our approach achieves separation of background cosmology and the effects of gravitation to all orders.

Separation of gravitational and non-gravitational aspects. Though the PDF constructed using the semi-analytical approaches does agree with numerical simulation that incorporates gravitation and adiabatic cooling, we also find departure from analytical prediction in the case of simulations with preheating. The non-gravitational processes that include preheating are not included in our analytical calculations. Thus,

departure from theoretical predictions provides a particularly interesting approach to separate out the effects of non-gravitational process on tSZ statistics.

Non-Gaussianity contribution from different baryonic components. We have studied the contribution to the tSZ effect from individual components such as the 'cold' gas $T < 10^5$ K, uncollapsed moderate overdense 'warm' gas $1 + \delta < 100$ and the total contribution from all components that include the intracluster gas within the haloes. We find that in addition to the total tSZ maps, the individual tSZ maps constructed using $T < 10^5$ K, $1 + \delta < 100$ components too can be described using our approach. For simulations with preheating we find a significant departure for the contribution from the 'warm' gas component $1 + \delta < 100$. The departure is more pronounced when the contributions from virialized haloes are included. However, we also find a near-perfect match for the contribution from the cold component.

Many previous studies have considered a halo-model-based approach for modelling of the gas distribution in collapsed, virialized objects. In this approach, the specific number density and the radial profile of these haloes are analysed using a PS formalism or its variants. However, detailed modelling of the complete PDF or the bias is possible in this approach only in an order-by-order manner. In our extended perturbative approach or the lognormal analysis, we go beyond the order-by-order approach and construct the entire cumulant generating function $\Phi(z)$ and relate it to that of the underlying density distribution $\phi(z)$. This allows us to reproduce and predict the entire PDF of the tSZ distribution for a specific smoothing angular scale. The statistical picture that we have developed here is complementary to that based on the PS formalism.

We would also like to point out that some previous studies have modelled the statistics of the tSZ effect using the hierarchical *ansatz* (Valageas & Silk 1999; Valageas et al. 2002). However, in these studies the contribution from individual haloes was computed using a virialization scheme and an equilibrium profile for the pressure distribution within the haloes. The results presented here are complementary to such prescriptions as we focus on the large-scale distribution of ionized gas. Instead of modelling the contribution from individual haloes, we directly link the baryonic pressure fluctuation responsible for the large-scale tSZ effect in terms of the underlying mass distribution.

We have ignored the presence of instrumental noise in our results. A beam-smoothed noise of the known PDF (Gaussian or otherwise) can always be convolved with the theoretical PDFs presented here before comparing them with any observational data. The method we pursue here also relies on having access to frequency-cleaned tSZ maps. The tSZ effect can also be studied using cross-correlation techniques that involve external tracers; such methods typically employ the 'mixed' bispectrum. The results, however, lack frequency information and are typically dominated by confusion noise. Using frequency-cleaned maps is expected to enhance the signal-to-noise ratio significantly by exploiting frequency information, in the absence of which the background CMB plays the role of intrinsic noise that degrades the signal-to-noise ratio. It is also interesting to note that the removal of tSZ signals from the CMB maps may actually help detection of other subdominant effects. The study of PDFs presented here can play an important role in this direction.

REFERENCES

Balian R., Schaeffer R., 1989, A&A, 220, 1
Bernardeau F., 1992, ApJ, 392, 1
Bernardeau F., 1994, A&A, 291, 697
Bernardeau F., 1996, A&A, 312, 11
Bernardeau F., Kofman L., 1995, ApJ, 443, 479
Bernardeau F., Schaeffer R., 1992, A&A, 255, 1
Bernardeau F., Schaeffer R., 1999, A&A, 349, 697
Bernardeau F., van Waerebek L., Mellier Y., 1997, A&A, 322, 1
Bernardeau F., Colombi S., Gaztanaga E., Scoccimarro R., 2002, Phys. Rep., 367, 1
Bi H. G., Davidson A. F., 1997, ApJ, 479, 523
Birkinshaw M., 1999, Phys. Rep., 310, 98
Borgani S., Viel M., 2009, MNRAS, 392, L26
Bouchet F. R., Gispert R., 1999, New Astron., 4, 443
Bouchet F., Strauss M. A., Davis M., Fisher K. B., Yahil A., Huchra J. P., 1993, ApJ, 417, 36
Cao L., Liu J., Fang L.-Z., 2007, ApJ, 661, 641
Coles P., Jones B., 1991, MNRAS, 248, 1
Coles P., Melott A., Munshi D., 1999, ApJ, 521, 5
Colombi S., 1994, ApJ, 435, L536
Colombi S., Bouchet F. R., Hernquist L., 1996, ApJ, 465, 14
Colombi S., Bernardeau F., Bouchet F. R., Hernquist L., 1997, MNRAS, 287, 241
Cooray A., 2000, Phys. Rev. D, 62, 103506

Cooray A., 2001b, Phys. Rev. D, 64, 063514
Cooray A., 2001a, Phys. Rev. D, 64, 043516
Cooray A., Seth R., 2002, Phys. Rep., 372, 1
Cooray A., Hu W., Tegmark M., 2000, ApJ, 540, 1
da Silva A., Barbosa A. C., Liddle A. R., Thomas P. A., 2000, MNRAS, 317, 37
Delabrouille J., Cardoso J., Patanchon G., 2003, MNRAS, 330, 807
Edward A. E., Henry J. P., 1991, ApJ, 383, 95
Fry J. N., 1984, ApJ, 279, 499
Goldberg D. M., Spergel D. N., 1999a, Phys. Rev. D, 59, 103001
Goldberg D. M., Spergel D. N., 1999b, Phys. Rev. D, 59, 103002
Hallman E. J., O'Shea B. W., Burns J. O., Norman M. L., Harkness R., Wagner R., 2007, ApJ, 671, 27
Hallman E. J., O'Shea B. W., Smith B. D., Burns J. O., Norman M. L., 2009, ApJ, 698, 1759
Hamilton A. J. S., 1985, ApJ, 292, L35
Hansen F., Branchini E., Mazzotta P., Cabella P., Dolag K., 2005, MNRAS, 361, 753
Hartley W. G., Gazzola L., Pearce F. R., Kay S. T., Thomas P. A., 2008, MNRAS, 386, 2015
Hill J. C., Sherwin B. D., 2012, arXiv:1205.5794
Hui L., 1999, ApJ, 519, L9
Joudaki S., Smidt J., Amblard A., Cooray A., 2010, J. Cosmol. Astropart. Phys., 1008, 027
Kaiser N., 1991, ApJ, 383, 104
Kaiser N., 1992, ApJ, 388, 272
Kay S. T., Liddle A. R., Thomas P., 2001, MNRAS, 325, 835
Kay S. T., Peel M. W., Short C. J., Thomas P. A., Young O. E., Battye R. A., Liddle A. R., Pearce F. R., 2012, MNRAS, 422, 1999
Kofman L., Bertschinger E., Gelb J. M., Nusser A., Dekel A., 1994, ApJ, 420, 44
Komatsu E., Seljak U., 2002, MNRAS, 336, 1256
Leach S. M. et al., 2008, A&A, 491, 597
Limber D. N., 1954, ApJ, 119, 665
Lin K.-Y, Woo T.-P., Tseng Y.-H., Lin L., Chiueh T., 2004, ApJ, 608, L1
Matarrese S., Lucchin F., Moscardini L, Saez D., 1992, MNRAS, 259, 437
Munshi D., 2000, MNRAS, 318, 145
Munshi D., Coles P., 2000, MNRAS, 313, 148
Munshi D., Jain B., 2000, MNRAS, 318, 109
Munshi D., Jain B., 2001, MNRAS, 322, 107
Munshi D., Sahni V., Starobinsky A., 1994, ApJ, 436, 517
Munshi D., Bernardeau F., Melott A. L., Schaeffer R., 1999, MNRAS, 303, 433
Munshi D., Coles P., Melott A., 1999a, MNRAS, 310, 892
Munshi D., Coles P., Melott A., 1999b, MNRAS, 307, 387
Munshi D., Melott A., Coles P., 2000, MNRAS, 311, 149
Munshi D., van Waerbeke L., Smidt J., Coles P., 2012, MNRAS, 419, 536
Navarro J., Frenk C., White S. D. M., 1996, ApJ, 462, 563
Peebles P. J. E., 1980, Large-Scale Structure of the Universe. Princeton Univ. Press, Princeton, NJ (ISBN: 9780691082400)
Persi F., Spergel D., Cen R., Ostriker J., 1995, ApJ, 442, 1
Press W. H., Schechter P., 1974, ApJ, 187, 425
Refregier A., Teyssier R., 2002, Phys. Rev. D, 66, 043002
Refregier A., Komatsu E., Spergel D. N., Pen U.-L., 2000, Phys. Rev. D, 61, 123001
Rephaeli Y., 1995, ARA&A, 33, 541
Roncarelli M., Moscardini L., Borgano S., Dolag K., 2007, MNRAS, 378, 1259
Runyan M. C. et al., 2003, ApJS, 149, 265
Schulz A. E., White M., 2003, ApJ, 586, 723
Scoccimarro R., Frieman J. A., 1999, ApJ, 520, 35
Seljak U., 2000, MNRAS, 318, 203
Seljak U., Burwell J., Pen U.-L., 2001, Phys. Rev. D, 63, 063001
Shange C., Crotts A., Haiman Z., 2007, ApJ, 671, 136
Short C. J., Thomas P. A., Young O. E., Pearce F. R., Jenkins A., Muanwong O., 2010, MNRAS, 408, 2213
Springel V., 2005, MNRAS, 364, 1105
Springel V., White M., Hernquist L., 2001, ApJ, 549, 681
Starek R., Rudd D., Evrard A. E., 2009, MNRAS, 394, L1
Sunyaev R. A., Zel'dovich Ya B., 1972, Comments Astrophys. Space Phys., 4, 173
Sunyaev R. A., Zel'dovich Ya B., 1980, ARA&A, 18, 537
Szapudi I., Colombi S., 1996, ApJ, 470, 131
Szapudi I., Szalay A. S., 1993, ApJ, 408, 43
Szapudi I., Szalay A. S., 1997, ApJ, 481, L1
Szapudi I., Szalay A. S., Boschan P., 1992, ApJ, 390, 350
Taruya A., Takada M., Hamana T., Kayo I., Futamase T., 2002, ApJ, 571, 638
The Planck Collaboration, 2006, astro-ph/0604069
Theuns T., Mo H. J., Schaye J., 2001, MNRAS, 321, 450
Valageas P., Munshi D., 2004, MNRAS, 354, 1146
Valageas P., Silk J., 1999, A&A, 347, 1
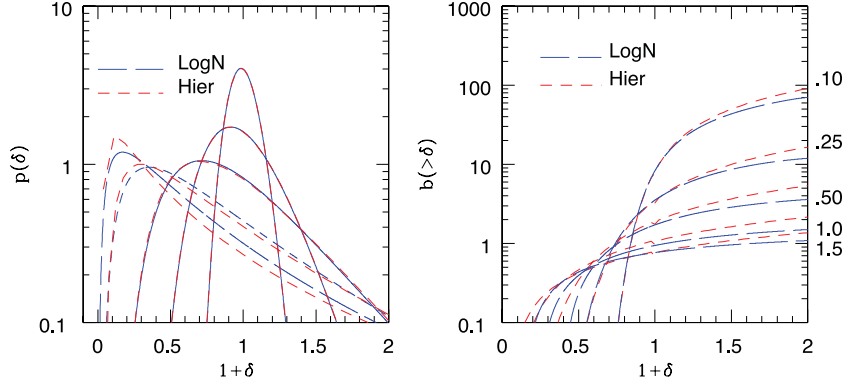Valageas P., Lacey C., Schaeffer R., 2000, MNRAS, 311, 234

Figure A1. The left-hand panel depicts PDF $p(\delta)$ as a function $1 + \delta$ for various values of $\sigma = 0.1, 0.25, 0.5, 1.0, 1.5$. Two different approximations are considered, the lognormal (long dashed) and the hierarchical ansatz (short dashed). The broader PDFs correspond to higher values of σ. The bias $b(> \delta)$ is plotted as a function $1 + \delta$ in the right-hand panel. Two different approximations are considered, the lognormal distribution (long dashed) and the hierarchical ansatz (short dashed). The analytical results correspond to the large-separation limit.

Valageas P., Schaeffer R., Silk J., 2002, A&A, 388, 741
Voit G. M., 2005, Rev. Mod. Phys., 77, 207
White S. D. M., 1979, MNRAS, 186, 145
White M., 2003, ApJ, 597, 650, 658
White M., Hernquist V., Springel V., 2002, ApJ, 579, 16
Young O. E., Thomas P. A., Short C. J., Pearce F., 2011, MNRAS, 413, 691
Zhang P., Pen U.-L., 2001, ApJ, 549, 18
Zhang P., Seth R. K., 2007, ApJ, 579, 16
Zhang P., Pen U.-L, Trac H., 2004, MNRAS, 355, 451

APPENDIX A: THE LOGNORMAL DISTRIBUTION

The evolution of PDF of the density field δ can also be modelled using the *lognormal* distribution. (Hamilton 1985; Coles & Jones 1991; Bouchet et al. 1993; Kofman et al. 1994). Detailed discussion of various issues involving of the lognormal distribution can be found in Bernardeau & Kofman (1995) and Colombi (1994). We will use the following expressions for the PDF $p(\delta)$ and the joint PDF $p(\delta_1, \delta_2)$ for our study (Taruya et al. 2002):

$$p(\delta)\mathrm{d}\delta = \frac{1}{\sqrt{2\pi\Sigma^2}} \exp\left[-\frac{\Lambda^2}{2\Sigma^2}\right] \frac{\mathrm{d}\delta}{1 + \delta}; \tag{A1}$$

$$\Sigma = \ln(1 + \sigma^2); \quad \Lambda = \ln[(1 + \delta)\sqrt{(1 + \sigma^2)}]; \tag{A2}$$

$$p(\delta_1, \delta_2)\,\mathrm{d}\delta_1\mathrm{d}\delta_2 = \frac{1}{2\pi\sqrt{\Sigma^2 - X_{12}^2}} \exp\left[-\frac{\Sigma(\Lambda_1^2 + \Lambda_2^2) - 2X_{12}\Lambda_1\Lambda_2}{2(\Sigma^2 - X_{12}^2)}\right] \frac{\mathrm{d}\delta_1}{1 + \delta_1} \frac{\mathrm{d}\delta_2}{1 + \delta_2}; \tag{A3}$$

$$\Lambda_i = \ln[(1 + \delta_i)\sqrt{(1 + \sigma^2)}]; \quad X_{12} = \ln(1 + \xi_\delta^{(2)}(r_1, r_2)). \tag{A4}$$

In the limiting case of large separation $X_{12} \to 0$ we can write down the two-point PDF as

$$p(\delta_1, \delta_2) = p(\delta_1)p(\delta_2)[1 + b(\delta_1)\xi_\delta^{(2)}(r_1, r_2)b(\delta_2)]; \qquad b(\delta_i) = \Lambda_i/\Sigma. \tag{A5}$$

It is however easier to estimate the cumulative or integrated bias associated with objects beyond a certain density threshold δ_0. This is defined as $b(\delta > \delta_0) = \int_{\delta_0}^{\infty} p(\delta)b(\delta)\,\mathrm{d}\delta / \int_{\delta_0}^{\infty} p(\delta)\,\mathrm{d}\delta$. In the low-variance limit $\sigma^2 \to 0$ the usual Gaussian result is restored $b(\delta) = \delta/\sigma^2$. The parameters $\Lambda, \Lambda_i, X_{12}, \Sigma$ that we have introduced above can be expressed in terms of the two-point (non-linear) correlation function $\xi_\delta^{(2)}(r_1, r_2) \equiv \langle\delta(r_1)\delta(r_2)\rangle \equiv \langle\delta_1\delta_2\rangle$ and the non-linear variance $\sigma^2 = \langle\delta^2\rangle$ of the smoothed density field. The lognormal distribution has already been used to model the statistics of weak-lensing observables (Munshi 2000; Taruya et al. 2002) and the clustering of Lyman α absorption systems (e.g. Bi & Davidson 1997), and is known to model gravitational clustering in the quasi-linear regime (Matarresse et al. 1992; Munshi et al. 1994). In Fig. A1 we compare the PDF and bias predictions from the lognormal model and hierarchical ansatz for various values of the variance. Though hierarchical ansatz and the lognormal model both predict nearly identical PDFs in the quasi-linear regime, it is important to realize that the lognormal model is *not* a member of the family of hierarchical models, i.e. the PDF of lognormal model cannot be cast into the form given in equation (23).

APPENDIX B: HIERARCHICAL ANSATZ (MINIMAL TREE MODEL): A VERY BRIEF REVIEW

As mentioned before, the PDF $p(\delta)$ and the bias $b(\delta)$ can both be constructed from the knowledge of the VPF $\phi(z) = \sum_{p=1} S_p z^p / p!$ and its two-point analogue $\tau(z) = \sum_p C_{p1} z^p / p!$. Here the parameters S_p and C_{p1} are normalized cumulants and cumulant correlators for the density field.

The modelling of $\phi(z)$ and $\tau(z)$ needs detailed knowledge of the entire correlation hierarchy. The detailed knowledge of the entire correlation hierarchy is encoded in the vertex generating function $\mathcal{G}(\tau)$). Typically for large values of y, the VPF exhibits a power law $\phi(z) = az^{1-\omega}$. The parameter typically takes a value of $\omega = 0.3$ for CDM-like spectra. There are no theoretical estimates of ω and it is generally estimated from numerical simulations. For small but negative values of y the functions $\phi(z)$ and $\tau(z)$ develop a singularity in the complex plane which is described by the following parametrization (Balian & Schaeffer 1989):

$$\phi(z) = \phi_s - a_s \Gamma(\omega_s)(z - z_s)^{-\omega_s}; \qquad \tau(z) = \tau_s - b_s(z - z_s)^{-\omega_s - 1}. \tag{B1}$$

The singularity structure of $\phi(z)$ and $\tau(z)$ depends on the nature of the vertex generating function $G(\tau)$ and its behaviour near the singularity τ_s (Balian & Schaeffer 1989):

$$a_s = \frac{1}{\Gamma(-1/2)} \mathcal{G}'(\tau_s)\mathcal{G}''(\tau_s) \left[\frac{2\mathcal{G}'(\tau_s)\mathcal{G}''(\tau_s)}{\mathcal{G}'''(\tau_s)} \right]^{3/2}; \qquad b_s = \left[\frac{2\mathcal{G}'(\tau_s)\mathcal{G}''(\tau_s)}{\mathcal{G}'''(\tau_s)} \right]^{1/2}. \tag{B2}$$

On the other hand, the parameters ω and a can be described in terms of a parameter z_s which in turn describes the exponential decay of the PDF for large density contrast δ (Balian & Schaeffer 1989):

$$\omega = \frac{k_a}{(k_a + 2)}, \; ; \qquad a = \frac{k_a + 2}{2} k_a^{k_a/k_a + 2}; \qquad -\frac{1}{z_s} = x_\star = \frac{1}{k_a} \frac{(k_a + 2)^{k_a + 2}}{(k_a + 1)^{k_a + 1}}. \tag{B3}$$

The PDF and the bias thus have two distinct regimes that are dictated by the two asymptotes. For intermediate values of δ, the PDF shows a power-law behaviour. The PDF and the bias are given by the following expression (Balian & Schaeffer 1989):

$$\bar{\xi}_2^{\frac{-\omega}{(1-\omega)}} \ll 1 + \delta \ll \bar{\xi}_2; \qquad p(\delta) = \frac{a}{\bar{\xi}_2^2} \frac{1-\omega}{\Gamma(\omega)} \left(\frac{1+\delta}{\bar{\xi}_2} \right)^{\omega-2}; \qquad b(\delta) = \left(\frac{\omega}{2a} \right)^{1/2} \frac{\Gamma(\omega)}{\Gamma[\frac{1}{2}(1+\omega)]} \left(\frac{1+\delta}{\bar{\xi}_2} \right)^{(1-\omega)/2}. \tag{B4}$$

For large values of δ, the PDF on the other hand shows an exponential behaviour (Balian & Schaeffer 1989):

$$1 + \delta \gg \bar{\xi}_2; \quad p(\delta) = \frac{a_s}{\bar{\xi}_2^2} \left(\frac{1+\delta}{\bar{\xi}_2} \right) \exp\left(-\frac{1+\delta}{x_\star \bar{\xi}_2} \right); \qquad b(\delta) = -\frac{1}{\mathcal{G}'(\tau_s)} \frac{(1+\delta)}{\bar{\xi}_2}. \tag{B5}$$

At very small values of δ, the PDF shows an exponential decay which is described only by the parameter ω (Balian & Schaeffer 1989):

$$1 + \delta \ll \bar{\xi}_2; \quad p(\delta) = a^{-1/(1-\omega)} \bar{\xi}_2^{\omega/(1-\omega)} \sqrt{\frac{(1-\omega)^{1/\omega}}{2\pi\omega v^{(1+\omega)/\omega}}} \exp\left[-\omega \left(\frac{v}{1-\omega} \right)^{-(1-\omega)/\omega} \right]; \tag{B6}$$
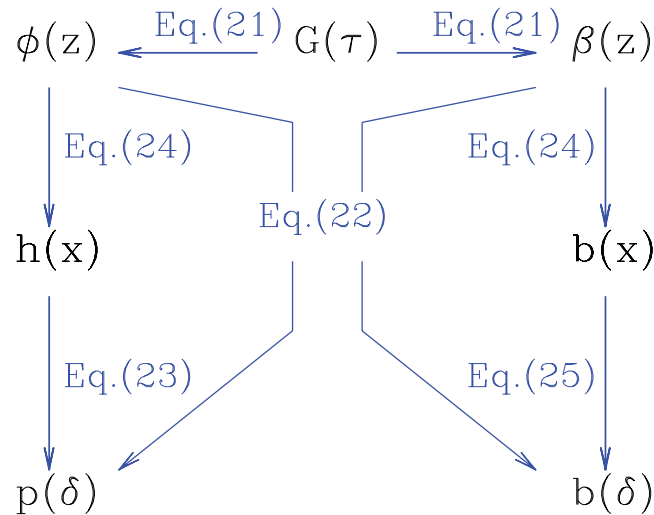

Figure B1. A simple 'flowchart' for a hierarchical approach is shown. It provides a summary of how the PDF $p(\delta)$ and bias $b(\delta)$ are constructed for a given model for the generating function $\mathcal{G}(\tau)$. The construction involves the generating function for the normalized cumulants or S_p parameters and cumulant correlators C_{pq}, i.e. $\phi(z)$ and $\beta(z)$. These are related to $p(\delta)$ and $b(\delta)$ through Laplace transforms. The scaling functions $h(x)$ and $b(x)$ encode the scaling properties of $p(\delta)$ and $b(\delta)$. We show the equation numbers that relate various quantities in the diagrams. The left-hand side of the diagram corresponds to one-point PDF and the right-hand side to the two-point PDF which is expressed through the bias function $b(\delta)$.

$$b(\delta) = -\left(\frac{2\omega}{\bar{\xi}_2}\right)^{1/2}\left(\frac{1-\omega}{v}\right)^{(1-\omega)/2\omega} ; \quad v = (1+\delta)[a]^{[-1/(1-\omega)]}[\bar{\xi}_2]^{[\omega/(1-\omega)]}. \tag{B7}$$

The range of δ for which the power-law regime is valid depends on the value of $\bar{\xi}_2$. For smaller values of $\bar{\xi}_2$, the power-law regime is less pronounced. A more detailed discussion of these issues can be found in Munshi et al. (1999). The links to the gravitational dynamics in the quasi-linear regime for various approximations are discussed in Munshi et al. (1994). In this paper we have considered only a specific version of the hierarchical ansatz known as the *minimal* tree model. This is the most popular version due to its simplicity; for variations and possible generalizations of the minimal tree model see Bernardeau & Schaeffer (1999). The equations that connect various generating functions with corresponding PDFs are shown in Fig. B1.

This paper has been typeset from a TEX/LATEX file prepared by the author.